

On the edge turbulence in a DTT-like tokamak plasma

F. Cianfrani¹ & G. Montani^{1,2}

¹ ENEA, Nuclear Department, C. R. Frascati, Via E. Fermi 45, 00044 Frascati (Roma), Italy

² Physics Department, “Sapienza” University of Rome, P.le Aldo Moro 5, 00185 Roma, Italy

E-mail: francesco.cianfrani@enea.it, giovanni.montani@enea.it

April 2024

Abstract. Turbulent transport provides the main contribution to particle and energy losses in tokamak plasmas, which control is of paramount importance for forthcoming reactors such as the Divertor-Tokamak-Test (DTT) facility under construction at ENEA Frascati. In this work we investigate the characteristic features of drift turbulence at the plasma edge through 3D electro-static fluid simulations. We outline the crucial role of the diffusion coefficient for the emerging turbulent spectra and for the excitation of vortex structures or zonal flows. Moreover, the impact of adding a poloidal magnetic component is discussed considering also a radial shear, and the emergence of anisotropic spectral features is emphasized. The analysis is extended to the case with Dirichlet boundary conditions along the radial direction, instead of the periodic ones usually employed in such kind of analyses.

1. Introduction

The confinement of particles and energy in the core of fusion plasmas is the main challenge for nuclear fusion research [1]. The realization of a spatial region with closed magnetic field lines (core) is the key aspect of tokamak reactors, in which a toroidal magnetic field is applied via external coils and a poloidal component is generated inductively through an electric discharge. The plasma core dynamics is characterized by violent instabilities and strong non-linearities, generating turbulent outward transport reducing confinement that can only be described via extremely costly (gyrokinetic) numerical simulations [2, 3]. The core is surrounded by the scrape-off-layer (SOL) in which the magnetic field lines open and can be tailored to form an X-point and drive most of the particle fluxes in the so-called divertor region where they impact some properly designed targets capable of sustaining large heat fluxes [4]. In order to test the divertor design for ITER and DEMO, the Divertor-Tokamak-Test facility (DTT) [5, 6] is being realized at ENEA laboratories in Frascati.

Physical conditions change moving from the core to SOL with increasing collisionality and decreasing energy/temperature/density, such that Braginski fluid models [7] with drift ordering [8] are expected to be viable and are commonly used by the most advanced global codes simulating edge plasma turbulence (as for instance BOUT++[9], GBS [10], TOKAMAK3X [11] and GRILLIX [12], see Ref.[13] for a recent review). These codes are aimed at predicting the profiles of the main physical quantities (density, temperature, electrostatic and magnetic potentials) measured in experiments accounting for the complicated wall features and magnetic geometries of real machines (see for instance [14]) and recently including also neutrals [15, 16, 17] to improve code validation in the divertor region.

The focus of the present work is complementary to these analyses: we want to provide an enhancement in the physical comprehension of tokamak edge plasma turbulence, by exploiting the impact of the adopted parameters and of the (X-point) magnetic geometry in a simplified context that could help interpreting the results of more comprehensive codes (as for instance turbulence suppression near the X-point [18], poloidal asymmetry [19], generation of sheared flows/electric fields [20], global vs local effects..).

The standard model for edge drift turbulence is the Hasegawa-Wakatani (HW) [21, 22, 23] (see also Ref.[24] for an historical review) system of equations, in which vorticity is subject to the Euler equation and density is passively advected on the $E \times B$ velocity field while the drift term couples the two equations through second order parallel gradients. Because of the anisotropy due to the background magnetic field 2D HW models are usually considered with an effective drift coupling obtained by replacing second parallel derivatives with the so-called adiabatic parameter. The seminal work [25] outlined the different behavior of 3D simulations with respect to effective 2D models. In 3D turbulence is sustained by the nonlinear transfer between $n = 0$ and $n \neq 0$ modes, the latter decaying in time such that turbulence quench and a poloidal flow tends to form (self-regulation). The analysis in Ref.[25] was performed in SLAB and hyperdiffusive and hyperviscous dissipation terms were adopted. A more complete model for edge tokamak plasma was investigated in Ref.[26], including electro-magnetic fluctuations, interchange instability and sheared magnetic geometry. The main achievement was the recognition that drift turbulence is a self-sustained process [27], *i.e.* that the presence of linear instability is not much relevant for the nonlinear regime, as mode saturated levels and energy transport are mostly determined by nonlinear mechanisms rather than by the broadening of linear instabilities (an assumption made for instance in the mixing length argument). It was also discussed the different role of nonlinear advection for vorticity and for pressure, with the latter providing sub-grid dissipation and the former redistribution to all modes sustaining turbulence.

Self-sustenance was the motivation for the reduced model of edge turbulence described in Refs.[28, 29, 30], in which the linear drive due to background pressure gradients was neglected and the HW system was reduced to a single equation for the electro-static potential only.

The generation of toroidally symmetric poloidal (zonal) flows [31, 32] has a crucial impact on turbulence. In particular, sheared flows break up short-scale vortex structures and suppress turbulence. This is accompanied by the formation of a sheared radial electric field and a transport barrier [33, 34]. In general, the fate of turbulence is affected by spectral symmetry. In fact, a symmetry breaking in the spectral correlator of collisional drift wave turbulence is known to produce finite residual (non-diffusive) Reynolds stress component whose divergence is responsible for the generation of momentum flows quenching turbulence [35, 36].

In this work, we study HW system of equations by performing fast 3D simulations in Fourier space and comparing the results varying the main linear parameters, namely the background pressure gradient length scale ℓ_0 and diffusivity χ_\perp . Particular attention is devoted to the dependence on the turbulence features on the value of the particle diffusion coefficient, *i.e.* Braginskii [7] and neoclassical [37] setups are considered. We will outline the different character of the resulting turbulent scenarios, in particular the achievement of toroidally symmetric and of poloidally symmetric configurations (zonal flows), the profiles of the resulting 2D spectra in the perpendicular plane and the development of anisotropic profiles, the role of toroidal transitions ($n \neq 0 \rightarrow n = 0$) in establishing the saturated energy spectra. In order to understand the impact of the magnetic geometry we consider three different magnetic configurations. The SLAB case in which the magnetic field is purely toroidal will set the benchmark scenarios for drift turbulence. By the addition of a constant poloidal component (limiter-like configuration), we will discuss the impact of a poloidal drift component on such scenarios, that is to provide anisotropic spectra and to modify the saturated behavior of toroidal transitions. The stabilizing role of shear [38] will finally be addressed by considering a radially sheared poloidal magnetic component, that will still lead to anisotropic spectra whose profiles will yet approach those in SLAB.

We will also consider nontrivial boundary conditions with respect to fully periodic ones inherent to the analysis in Fourier space. In fact, we will show how vanishing Dirichlet boundary conditions can be realized through a formulation in terms of the sine Fourier transform. This procedure will be implemented along the radial direction and will produce a further source of spectral anisotropy, and partial turbulence quench, that can be understood in terms of symmetry breaking due to the different boundary conditions for the radial coordinate and the poloidal angle.

The main merit of this manuscript is in outlining that in the neoclassical regime of particle transport the basic drift coupling mechanism underlying self-sustained turbulence is suppressed in favor of the formation of toroidally and poloidally symmetric structures.

The organization of the work is as follows. In section 2 the basic equations for the edge turbulence model are presented, while in subsection 2.1 the numerical integration scheme is described. The simulation results are shown in section 3, with the different considered magnetic geometries discussed in next subsections: SLAB in subsection 3.1, constant and radially sheared poloidal magnetic components in subsections 3.2 and 3.3,

respectively. In section 4 concluding remarks follow.

2. Basic equations and methodology

Drift turbulence in the edge plasma region can be described in the low frequency limit ($\omega \ll \Omega_i$, Ω_i being ion cyclotron frequency) using the fluid description with drift-ordering approximation. Assuming charge neutrality, equal electron and ion temperatures $T_e = T_i = T$ and a background pressure p_0 , such that the total pressure $p = p_0 + \tilde{p}$, the variables are the electro-static potential ϕ , the perturbed pressure \tilde{p} , the magnetic potential ψ and the parallel fluid velocity v_{\parallel} . Discarding v_{\parallel} and parallel diffusivity, the basic equations can be derived from charge neutrality, energy balance and generalized Ohm's law resulting in [39, 29]

$$\begin{cases} \partial_t \Delta_{\perp} \phi + \{\phi, \Delta_{\perp} \phi\} = B \nabla_{\parallel} (\Delta_{\perp} \psi) + \mu \Delta_{\perp}^2 \phi \\ \partial_t \tilde{p} + \{\phi, \tilde{p}\} = -\hat{k} \delta_y \phi + D \nabla_{\parallel} (\Delta_{\perp} \psi) + \chi_{\perp} \Delta_{\perp} \tilde{p} \\ \partial_t \psi = F \nabla_{\parallel} (\tilde{p} - \phi) + \eta \Delta_{\perp} \psi \end{cases} \quad (1)$$

where ion diamagnetic velocity and magnetic (curvature and gradient) drifts have been neglected. Parallel gradient ∇_{\parallel} appears in those terms accounting for drift response on the right-hand sides of the equations above and they are defined with respect to the magnetic geometry via the corresponding unit vector $\hat{b} = \vec{B}/B$

$$\nabla_{\parallel} = \hat{b}_x \partial_x + \hat{b}_y \partial_y + \hat{b}_z \partial_z, \quad (2)$$

with x , y and z local Cartesian coordinates for the radial, poloidal and toroidal direction, respectively. The perpendicular Laplacian reads

$$\Delta_{\perp} = \Delta - (\nabla_{\parallel})^2, \quad (3)$$

and it determines vorticity $\Delta_{\perp} \phi$ and the dissipative contributions.

The second terms on the left-hand side of the first two equations in (1) provide the advection by $\mathbf{E} \times \mathbf{B}$ drift and are written in terms of the Poisson brackets

$$\{f, g\} = \delta_x f \delta_y g - \delta_x g \delta_y f \quad (4)$$

δ_x and δ_y being the corresponding derivative operators projected onto the perpendicular plane to the magnetic field. The first term on the right-hand side of the equation for \tilde{p} is due to the background pressure gradients since $\hat{k} = \delta_x p_0$ and it provides a free-energy source for turbulence. In what follows, a linear background pressure profile is assumed, such that $\hat{k} = \delta_x p_0 \sim \partial_x p_0 = 1/\ell_0$ can be taken as a constant with $1/\ell_0$ specifying the magnitude of p_0 gradient.

The last terms on the right-hand side of Eqs.(1) are dissipative. In what follows, the corresponding parameters, namely viscosity μ , diffusivity χ_{\perp} and resistivity η , are all fixed according with Braginskii values, except for χ_{\perp} for which also a value ten times larger is considered representing the neoclassical case $\chi_{\text{neocl}} = 10\chi_{\text{class}}$.

In the electro-static limit, one can assume $\partial_t \psi \sim 0$ and compute $J_{\parallel} = \Delta_{\perp} \psi$ from the generalized Ohm's law so getting the reduced set of equations

$$\begin{cases} \partial_t \Delta_{\perp} \phi + \{\phi, \Delta_{\perp} \phi\} = \frac{BF}{\eta} \nabla_{\parallel}^2 (\tilde{p} - \phi) + \mu \Delta_{\perp}^2 \phi \\ \partial_t \tilde{p} + \{\phi, \tilde{p}\} = -\hat{k} \delta_y \phi + \frac{DF}{\eta} \nabla_{\parallel}^2 (\tilde{p} - \phi) + \chi_{\perp} \Delta_{\perp} \tilde{p} \end{cases} \quad (5)$$

A typical DTT-like scenario is considered having [5]

$$n_0 = 5 \cdot 10^{-13} \text{cm}^{-3} \quad T = 100 \text{eV}, \quad B = 3T \quad R = 2.14 \text{m} \quad a = 68 \text{cm}. \quad (6)$$

n_0 being the background number density, R and a the major and minor tokamak radius, respectively. The corresponding Braginskii dissipative parameter χ_{\perp} read

$$\chi_{\perp} = \chi_{\text{class}} = 110 \text{cm}^2/\text{s}. \quad (7)$$

The electro-static and magnetic potential are normalized with $e/K_B T$, K_B being the Boltzmann constant, and pressure with $n_0 K_B T$. A fully-toroidal local poloidal section in the form of a 2cm side square is simulated in what follows neglecting any curvature effect. Cartesian coordinates are rescaled as $x, y \rightarrow x/L_{\perp}, y/L_{\perp}$ and $z \rightarrow z/L_{\parallel}$ such that rescaled coordinates range in the interval [0,10].

2.1. Numerical scheme

The system of equations (5) is solved using the explicit 4th order Runge-Kutta method in Fourier space (FS). At each iteration \tilde{p} and vorticity are advanced, while the electrostatic potential is computed by inverting Δ_{\perp} in FS. All the nonlinear terms are computed in real space and pulled-back in FS (pseudospectral method). The simulations are run in python that contains the *scipy* package providing an efficient implementation of the Fast Fourier Transforms (FFT) algorithm to move quickly back and forth to real space.

The description in FS naturally provides periodic boundary conditions (BC) for all the coordinates. However, we also implement vanishing Dirichlet BC in the x radial direction. This is done by restricting to x sine Fourier transform, such that the resulting field profiles are skew-symmetric under reflection along the midpoint $\ell_x/2$ of the simulation domain and vanish in 0 and $\ell_x/2$ (see Fig.1). All the background quantities, namely the background pressure gradient and the magnetic configuration, are taken symmetric under the same kind of reflection so preserving fields skew-symmetry along x in time and obtaining a solution of the considered problem with vanishing Dirichlet BC on half of the simulation domain.

The chosen initial conditions are 3D Gaussian wave packets centered inside the simulation domain as shown in Fig.2 with $\phi = \tilde{p}$ to minimize initial drift response. The initial values are such that turbulence is self-sustained [27], *i.e.* it is not seed by a linear unstable phase. We consider two cases for background pressure with $\ell_0 = 2\text{cm}$ and $\ell_0 = 10\text{cm}$ denoted as strong and weak gradients, respectively. Ignoring the role of the magnetic geometry (*i.e.* the stabilizing contribution of shear), a linear unstable spectral region is present in the former case, while all the modes are stable in the latter. In both

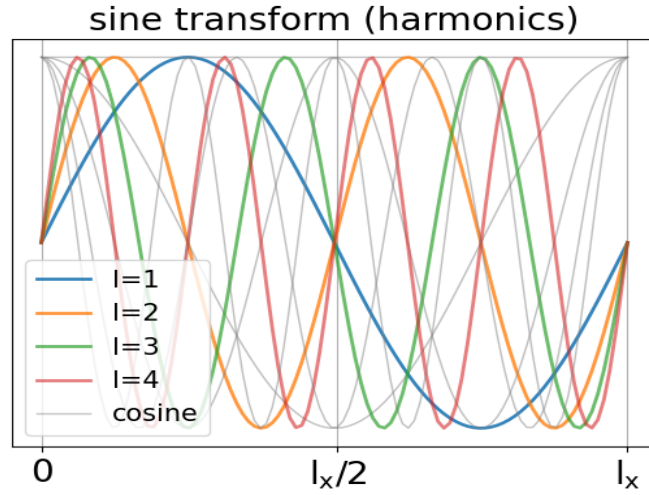


Figure 1. The first four sine (blue, orange, green and red lines) and cosine (light grey lines) harmonics in the radial simulation domain. Sine functions vanish at the boundary $x = 0, \ell_x$ and at the midpoint $x = \ell_x/2$. The profile in the second half is a specular copy of that in the first half with the mirror placed at the midpoint.

cases we will see turbulent behavior. Linear spectral analysis can be done analytically (see for instance [42]). A linear phase has here been found by reducing the magnitude of the initial condition and it has been used for benchmarking.

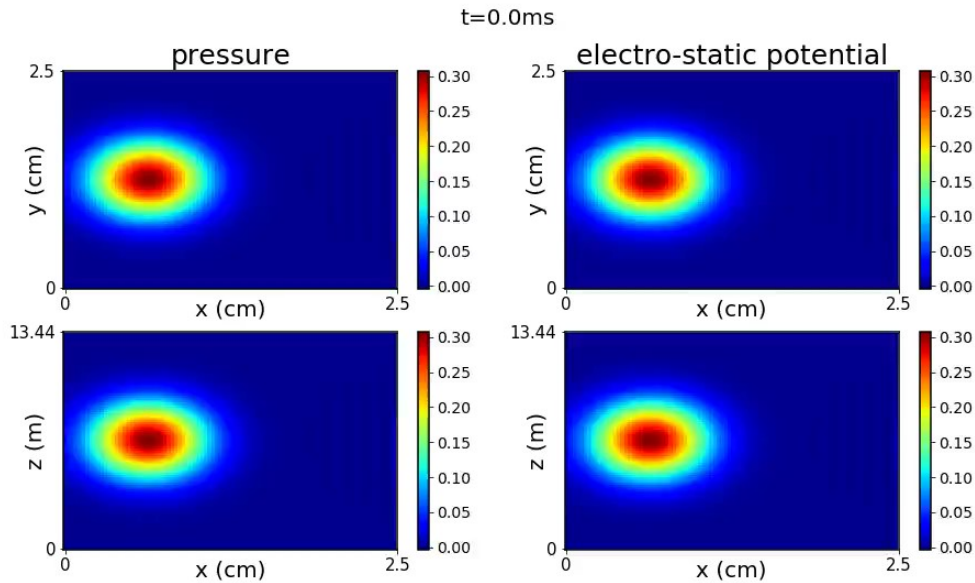


Figure 2. The 3D Gaussian functions taken as initial conditions of the simulations: the first row contains the poloidal sections, (x, y) plane, of normalized \tilde{p} (left) and ϕ (right) while the second row is for the radial-toroidal (x, z) plane. The corresponding colorbars are shown next to each plot.

Two values for diffusivity are discussed: Braginskii (classical case, χ_{class}) and ten times larger, that is representative of the neo-classical value $\chi_{\text{neocl}} = 10\chi_{\text{class}}$. We will emphasize the different behavior of turbulent spectra in such two cases. The value of perpendicular diffusivity in turbulent tokamak edge plasma simulations is usually fixed in order to reproduce expected features (pressure and density profiles) or to avoid numerical instabilities [43] and not according to a self-consistent procedure. This is due to the expectation that turbulent transport dominates diffusivity so that the bare diffusivity value can be ignored. Here we will outline how the resulting turbulence is strongly affected by the choice of classical or neoclassical diffusivity, suggesting that the chosen value of bare diffusivity may indeed play a role in determining the fate of turbulence and the emerging particle and energy transport.

The results for three magnetic poloidal configurations in addition to the constant toroidal component are presented in the next sections: vanishing (SLAB), constant and radially sheared fields. In the first two cases all \hat{b} components are constant (no shear) and ϕ is analytically derived from vorticity. Advection terms contain the products of two field derivatives that are computed in real space and pulled back to FS with FFT. Aliasing error is avoided by explicit zero padding for one third of the modes (implicit padding can be used for MPI implementations that are not considered here [40]).

In the last case magnetic shear is present. The Laplacian and its inverse are numerically pre-computed before starting the iteration. The drift terms contain the expression $\nabla_{\parallel}(\tilde{p} - \phi) = \hat{b} \cdot \vec{\nabla}(\tilde{p} - \phi)$ and since \hat{b} is not constant they are treated just like nonlinear advection in those cases without shear, *i.e.* $(\tilde{p} - \phi)$ gradients are mapped to real space, multiplied times \hat{b} components and finally pulled back to FS. The advection terms are now given by the product two fields and one geometric function, obtained by expanding δ_x and δ_y in x, y, z derivatives, resulting in a stronger mode restriction to avoid aliasing error (zero padding for half of the modes). These operations provide longer running time and larger memory usage in the case with shear. A good balance between lowering time/memory consumption and covering all the physically significant modes is obtained using $56 \times 56 \times 24$ modes, such that even in those cases with shear one reaches physical length scales down to just 3 times the Larmor radius (for $l, m = \pm 14$, l and m being radial and poloidal mode numbers).

3. Results

The simulation results for the three magnetic configurations described above are presented in the following subsections. The resulting turbulence features are discussed by outlining the role of the linear and the nonlinear contributions. In particular, we will derive the spectra of the energies E_{ϕ} , $E_{\tilde{p}}$ defined as

$$E_{\phi}(\vec{k}) = \frac{1}{2} |\nabla_{\perp} \phi|^2(\vec{k}) \quad E_{\tilde{p}}(\vec{k}) = \frac{1}{2} |\tilde{p}(\vec{k})|^2 \quad (8)$$

and of the corresponding fluxes

$$\begin{cases} \partial_t E_\phi = T_\phi + \Gamma_{\text{drift},\phi} - \Gamma_{\text{visc}} \\ \partial_t E_{\tilde{p}} = T_{\tilde{p}} + \Gamma_{\hat{k}} + \Gamma_{\text{drift},\tilde{p}} - \Gamma_{\text{diff}} \end{cases} \quad (9)$$

where the two drift contributions have no definite sign \ddagger and read

$$\begin{aligned} \Gamma_{\text{drift},\phi}(\vec{k}) &= -\frac{BF}{\eta} \phi(-\vec{k}) \nabla_{\parallel}^2 (\tilde{p} - \phi)(\vec{k}) \\ \Gamma_{\text{drift},\tilde{p}}(\vec{k}) &= \frac{DF}{\eta} \tilde{p}(-\vec{k}) \nabla_{\parallel}^2 (\tilde{p} - \phi)(\vec{k}), \end{aligned} \quad (10)$$

while the flux due to the background-pressure gradient is given by the expression

$$\Gamma_{\hat{k}}(\vec{k}) = -\hat{k} \tilde{p}(-\vec{k}) \delta_y \phi(\vec{k}), \quad (11)$$

and the two dissipative terms have the minus signs corresponding to the viscous and the diffusive ones, *i.e.*

$$\Gamma_{\text{visc}} = \nu |\Delta_{\perp} \phi(\vec{k})|^2 \quad \Gamma_{\text{diff}} = \chi_{\perp} |\nabla_{\perp} \tilde{p}(\vec{k})|^2. \quad (12)$$

All the derivative terms above (namely $\nabla_{\perp} \phi$, $\nabla_{\parallel} (\tilde{p} - \phi)$, $\delta_y \phi$, ..) can be written in FS as simple multiplicative operators ($ik_{\perp} \phi(\vec{k})$, $-k_{\parallel} (\tilde{p} - \phi)(\vec{k})$, $ik_y \phi(\vec{k})$, ..) only in the two cases without shear, while in the case with shear they are computed going back and forth to real space as described at the end of the previous section, mimicking the procedure adopted for the nonlinear transfer functions T_ϕ and $T_{\tilde{p}}$, whose expressions read

$$T_\phi(\vec{k}) = \phi(-\vec{k}) \{\phi, \Delta_{\perp} \phi\}(\vec{k}) \quad T_{\tilde{p}}(\vec{k}) = \tilde{p}(-\vec{k}) \{\phi, \tilde{p}\}(\vec{k}). \quad (13)$$

In what follows we will discuss the toroidal cascade to axisymmetric $n = 0$ modes, corresponding to $k_z = 0$. In this respect, we will split the nonlinear contribution into the 2D part $T_{\dots}^{(2D)}$, in which all the fields in Eqs.(13) are computed at $n = 0$, and the remaining part $T_{\dots}^{(n \neq 0 \rightarrow n=0)}$ giving the amount of transition from $n \neq 0$ to $n = 0$,

$$T_{\dots}(k_x, k_y, 0) = T_{\dots}^{(2D)}(k_x, k_y) + T_{\dots}^{(n \neq 0 \rightarrow n=0)}(k_x, k_y). \quad (14)$$

The basic free-energy flow goes as follows. $\Gamma_{\hat{k}}$ provides a free-energy source for $E_{\tilde{p}}$ whose magnitude is proportional to \hat{k} and is modulated by $\delta_y \phi$, then such energy redistributes by toroidal and poloidal cascades while being dissipated by diffusion. The drift term provides at the same time dissipation and a two-way flow between $E_{\tilde{p}}$ and E_ϕ with the latter being redistributed by poloidal and toroidal cascades and dissipated by viscosity.

\ddagger A generalized energy $E_\phi + (B/D) E_{\tilde{p}}$ can be defined for which the overall drift contribution is dissipative. We will not introduce it since we want to keep separated the contributions for ϕ and \tilde{p} as they correspond to different physical quantities in tokamak experiments with dedicated measurement apparatus.

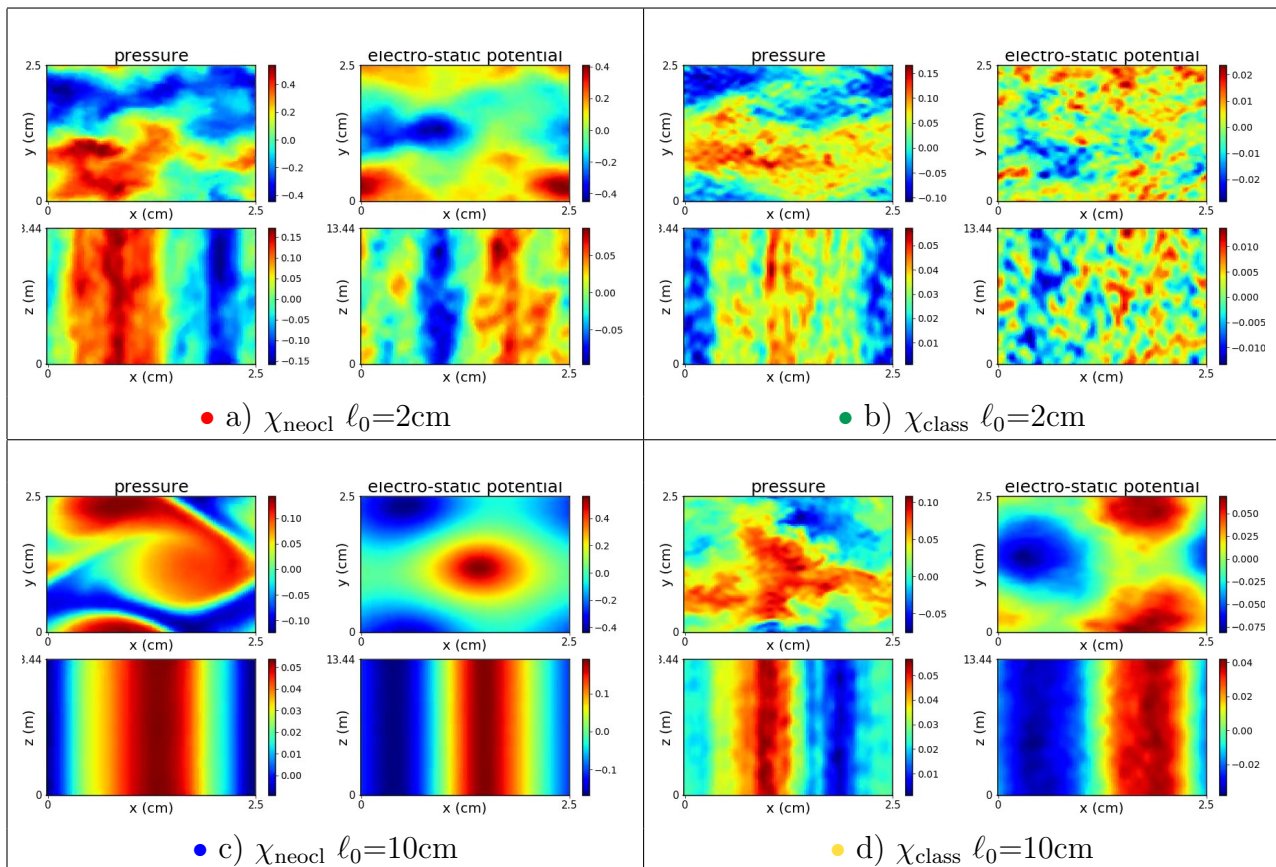


Table 1. The simulation results at time $t = 0.167\text{ms}$ in SLAB for fully periodic BC. In each panel the figures above contains the poloidal sections, (x, y) plane, of normalized \tilde{p} (left) and ϕ (right) while the figures below are for the radial-toroidal (x, z) plane. The corresponding colorbars are shown next to each plot.

3.1. SLAB

The SLAB case is characterized by fully toroidal magnetic field with $\hat{b}_x = \hat{b}_y = 0$ and $\hat{b}_z = 1$. The perpendicular Laplacian operator in FS is $\Delta_{\perp} = -(k_x^2 + k_y^2)$, the drift term vanishes for axisymmetric $n = 0$ modes and the free-energy source $\Gamma_{\hat{k}}$ is proportional to the poloidal number m .

The simulation results are shown in the multi-panel figure Tab.1, where in each panel the values of \tilde{p} and ϕ are shown at a given time $t = 0.167\text{ms}$ in the poloidal plane (x, y) (figures above) and in the radial-toroidal plane (x, z) (figures below). The two upper/lower panels are obtained for strong/weak background pressure gradient $\ell_0 = 2\text{cm}/\ell_0 = 10\text{cm}$ with neoclassical (left) and classical (right) diffusivity coefficients χ_{\perp} .

It is worth noting how both the perturbed pressure and electro-static potential reach an axisymmetric configuration in case c) (left bottom panel in Tab.1) with the formation of large vortex structures in the poloidal plane. Increasing background pressure gradient (bottom to top) or decreasing diffusivity (left to right) provides a large degree of toroidal asymmetry and the formation of small scale structures in the poloidal plane. These

qualitative features are common to all the considered magnetic geometries (see below).

The fraction of toroidally symmetric mode is shown in figure 3, where the ratios of $n = 0$ (solid lines) and $n = m = 0$ (dash-dotted lines) to total mode amplitude are plotted in time for the four considered cases. The former reaches saturated values for both ϕ and \tilde{p} that are practically one in case c) (blue) and very close to one in case d) (yellow), outlining how increasing diffusivity reduces the fraction of toroidally asymmetric modes. This is even more evident for ϕ amplitude in those cases (a) and b)) with strong background pressure gradients. In fact, in the neoclassical case a) (red) toroidally asymmetric modes are still strongly suppressed with more than $\sim 80\%$ of ϕ amplitudes at $n = 0$, while the same ratio reduces to just $\sim 20\%$ in case b) (green). The fraction of $n = 0$ modes that are also poloidally symmetric ($m = 0$) are plotted with dash-dotted lines and their saturated values oscillate around $1/3$ and one half of total $n = 0$ mode amplitude for \tilde{p} and ϕ , respectively.

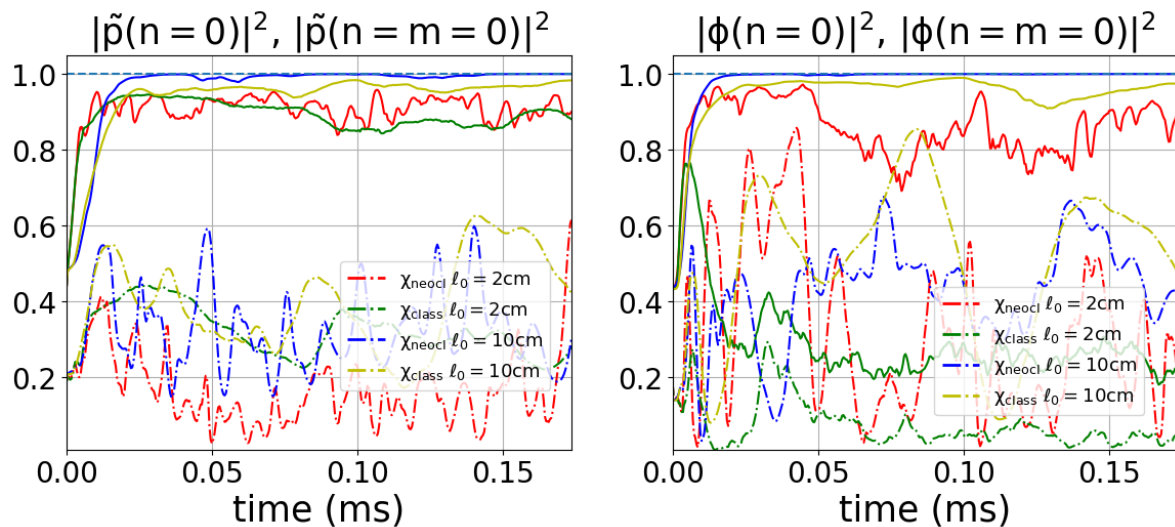


Figure 3. The ratio of $n = 0$ (solid lines) and of $n = m = 0$ (dash-dotted lines) mode amplitudes over the total amplitude for \tilde{p} (left) and ϕ (right) vs time (in ms) for the four considered cases in SLAB with fully periodic BC.

The energy spectra at $n = 0$ for \tilde{p} and ϕ are presented in Fig.4. In order to see potential anisotropies, it is shown the scatter plot for all the $(k_{\perp}\rho)^2$ values obtained from the computational discrete Cartesian grid in FS (anisotropies would appear as different spectral values for the same $(k_{\perp}\rho)^2$). The 2D spectra are indeed quite isotropic and show a strong dependence on the chosen parameters. In particular, for short wavelengths ($k_{\perp}\rho > 1$) E_{ϕ} goes as $\sim 1/k_{\perp}$ in case b) (green), $\sim 1/k_{\perp}^2$ in case d) (yellow) and $1/k_{\perp}^3$ in case a) (red) and the corresponding $E_{\tilde{p}}$ spectra are suppressed by a factor $1/k_{\perp}$. The spectra for case c) (blue) decays more rapidly with $k_{\perp}\rho$ and differently from the others, that are quite stationary, it becomes even more peaked moving forward the time window.

In order to understand the impact of 3D toroidal transitions on 2D spectra, we

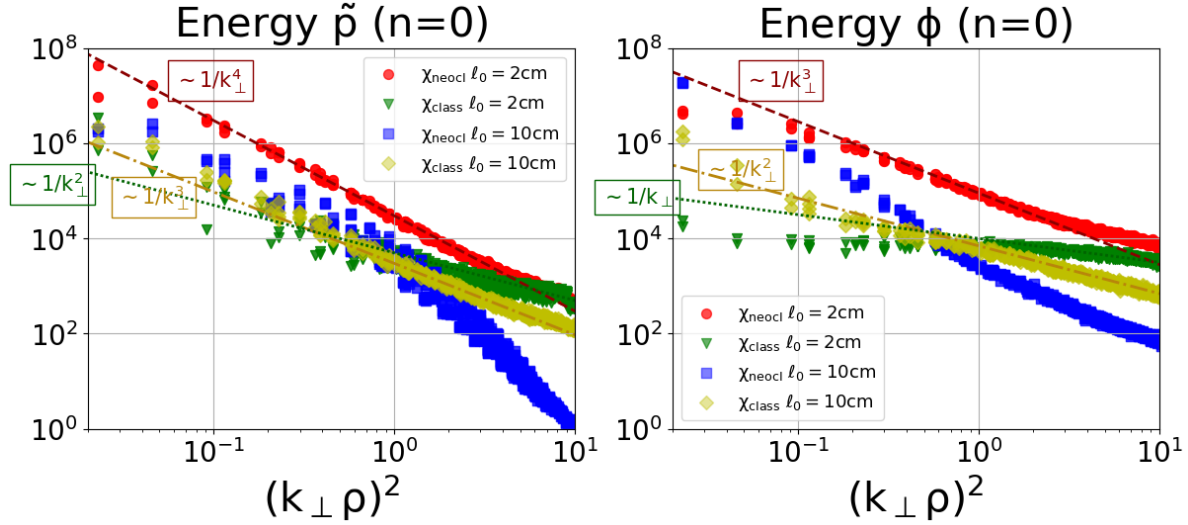


Figure 4. The scatter plots of normalized axisymmetric spectral energies $E_{\tilde{p}}$ (left) and E_{ϕ} (right) vs $(k_{\perp}\rho)^2$ for the four considered cases in SLAB with fully periodic BC. They are computed by averaging over a time window of $\sim 0.13ms$. Some curves are also plotted that approximate quite well some of the spectra profiles and which behave as: $1/k_{\perp}^4$ (dashed dark red line), $1/k_{\perp}^3$ (dash-dotted dark yellow line) and $1/k_{\perp}^2$ (dotted dark green line) for $E_{\tilde{p}}$ (left) and $1/k_{\perp}^3$ (dashed dark red line), $1/k_{\perp}^2$ (dash-dotted dark yellow line) and $1/k_{\perp}$ (dotted dark green line) for E_{ϕ} (right).

plot in Fig.5 the nonlinear transfer functions $T_{\tilde{p}}^{(n \neq 0 \rightarrow n=0)}$ (left) and $T_{\phi}^{(n \neq 0 \rightarrow n=0)}$ (right) accounting for the transitions from $n \neq 0$ to $n = 0$. We adopt a logarithmic sampling for $(k_{\perp}\rho)^2$ for readability. Each transfer function is normalized with the corresponding dissipative contribution (Γ_{diff} for \tilde{p} and Γ_{visc} for ϕ).

It is worth noting that $T_{\tilde{p}}^{(n \neq 0 \rightarrow n=0)}$ is negative, thus $n \neq 0$ modes behave as a sink (direct toroidal cascade) for pressure that is more intense by increasing background pressure gradients (green and red vs yellow and blue) and reducing diffusivity (blue and red vs yellow and green). In particular, for large part of the k_{\perp} spectrum $T_{\tilde{p}}^{(n \neq 0 \rightarrow n=0)} < -1$ meaning that it is larger than diffusion thus it is the main dissipative contribution partially compensating the source due to background pressure gradients $\Gamma_{\hat{k}}$ shown in dashed lines in Fig.5 (left). The corresponding 2D transition functions are shown in fig.6 (left). They increase from negative to positive values while increasing k_{\perp} , thus they provide an energy flow from large to small wave-lengths.

On the contrary, $T_{\phi}^{(n \neq 0 \rightarrow n=0)}$ has no definite sign and it plays the role of source or sink depending on the sampled k_{\perp} value and on the considered case. We can notice how it is close to 1 for $k_{\perp}\rho > 1$ in case d) (yellow), signaling that there is an inverse toroidal cascade partially compensating the viscous contribution and making the energy spectrum close to a pure 2D Euler inviscid one ($\sim 1/k_{\perp}^2$, Kraichman-Kolmogorow spectrum [41]§ obtained for the reduced drift turbulence model in Ref.[28]). In the same

§ A factor $1/k_{\perp}$ is due to the transformation from Cartesian k_x, k_y to cylindrical coordinates, reproducing the well-known formula $1/k_{\perp}^3$.

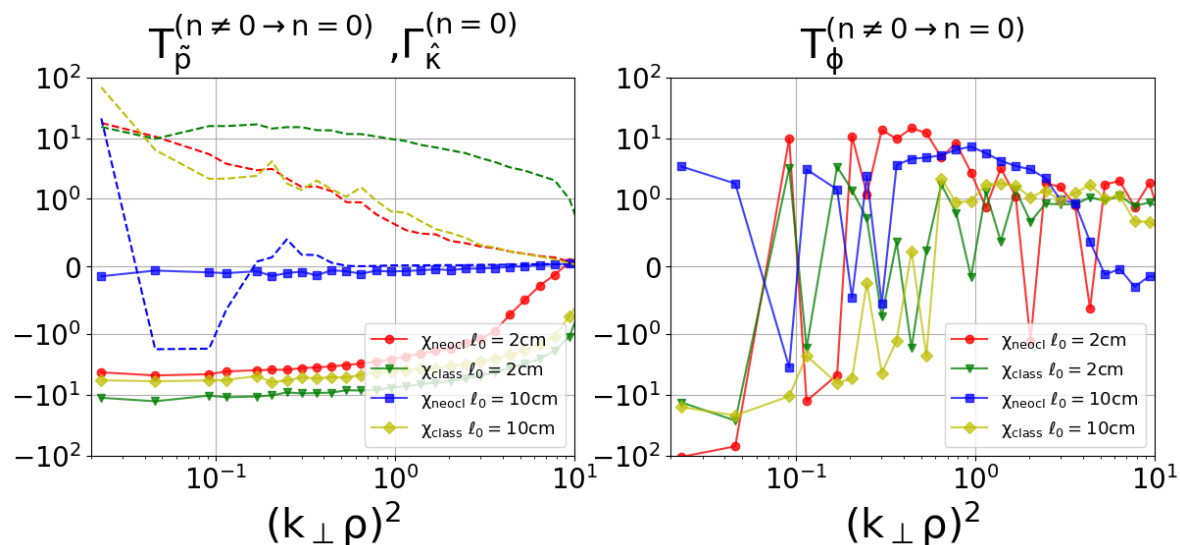


Figure 5. The nonlinear transfer functions of toroidal transitions $n \neq 0 \rightarrow n = 0$ (solid lines) for \tilde{p} (left) and ϕ (right) vs $(k_{\perp} \rho)^2$ and the flux due to background pressure gradient (dashed lines, left) for the four considered cases in SLAB with fully periodic BC. Each plotted value is normalized with the corresponding dissipative flux, *i.e.* the diffusivity and the viscous contributions for \tilde{p} and ϕ , respectively. The chosen values of $(k_{\perp} \rho)^2$ are constructed from the computational Cartesian grid in FS by taking the five smallest values of k_{\perp} and by logarithmically sampling the relic part.

part of the spectrum the red curve exhibits strong fluctuations around 0 amplitude, thus the overall contribution of the nonlinear toroidal transfers is smaller than one and this could explain the behavior $E_{\phi} \sim 1/k_{\perp}^3$ (Saffman spectrum [44], see the footnote). For smaller wave-numbers toroidal and 2D transfer functions (the latter shown in Fig.6) are strongly anticorrelated with large fluctuations between neighbor sampled k_{\perp} values. This means that 3D transitions are as relevant as 2D ones in determining the 2D energy spectra in Fig.4.

In case c) (blue) one notices that the direct toroidal cascade for \tilde{p} is very low, while there is an inverse toroidal cascade for most of ϕ spectra, leading to the axisymmetric profiles in table 1 and strongly peaked spectra in Fig.4. In other words, the free-energy source is low (weak p_0 gradients) and dissipation is high (neoclassical diffusivity), such that the turbulent source $\Gamma_{\hat{k}}$ is not able to sustain the toroidal cascades and thus drift turbulence decays. In fact, this case is far from stationary, with axisymmetric modes growing at the expenses of asymmetric ones and the 2D spectra getting more and more stiff (condensation).

This is accompanied by the formation of a radially-sheared electric field, that seeds further turbulence quench, as shown in Fig.7 where the toroidally and poloidally averaged radial electric field (solid lines) and the corresponding range of variability around the average (shaded regions) is plot along the x radial direction at four time values. An averaged sheared profile arises from the start (blue) to the end (red) of the simulation with the shaded region getting narrow with time signaling decreasing

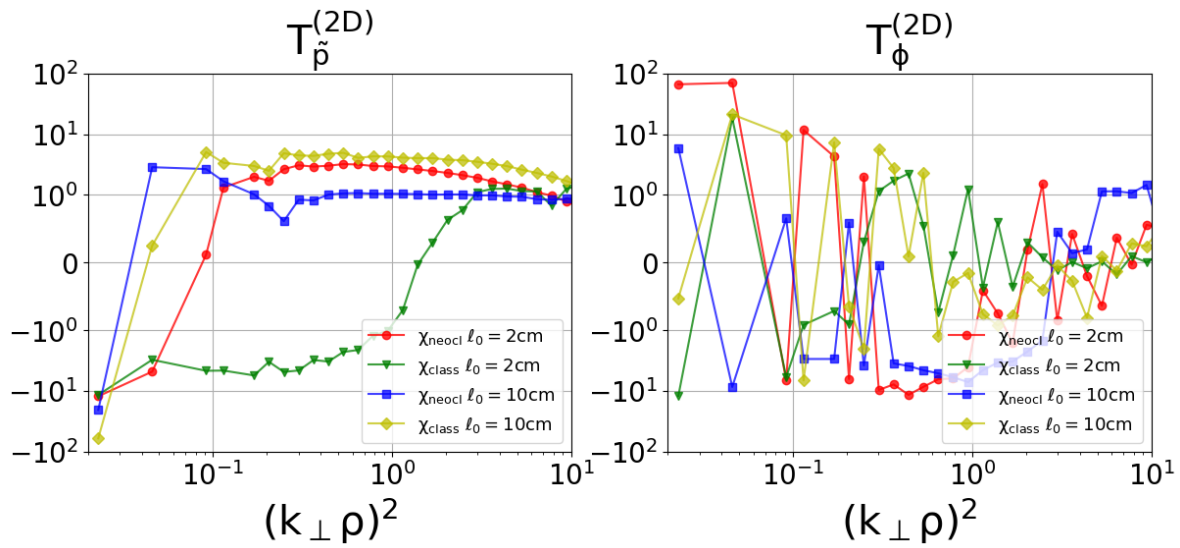


Figure 6. The nonlinear transfer functions of 2D transitions $n = 0 \rightarrow n = 0$ (solid lines) for \tilde{p} (left) and ϕ (right) vs $(k_{\perp}\rho)^2$ for the four considered cases in SLAB with fully periodic BC. Each plotted value is normalized with the corresponding dissipative flux, *i.e.* the diffusivity and the viscous contributions for \tilde{p} and ϕ , respectively.

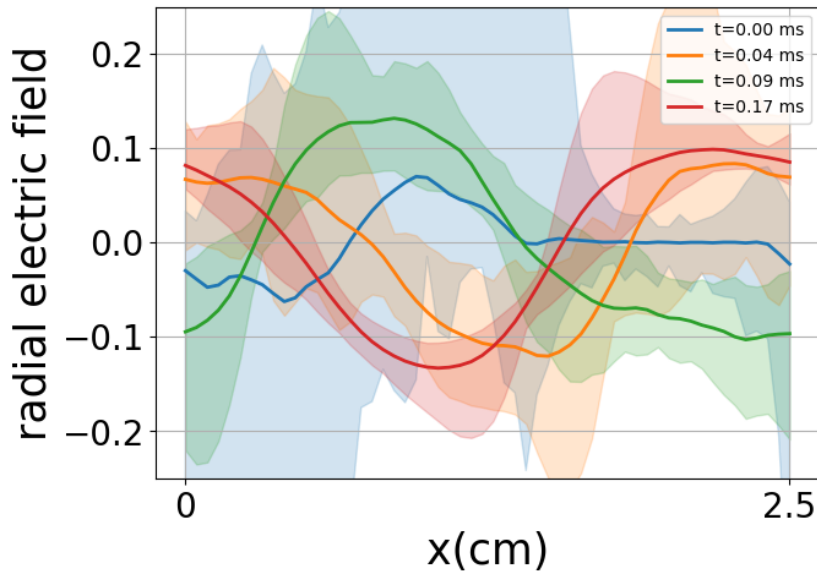


Figure 7. The profile of the radial electric field in case c) at four given time values: start (blue), $t = 0.04ms$ (orange), $t = 0.09ms$ (green) and $t = 0.17ms$ (red). The solid lines denote the averaged value along y and z directions, while the corresponding shaded regions cover the whole range of variability along such directions at the given time values.

variations from average along poloidal and toroidal directions.

3.1.1. Dirichlet BC The results for the simulations in SLAB with vanishing radial Dirichlet BC implemented through the method discussed in section 2 are presented in

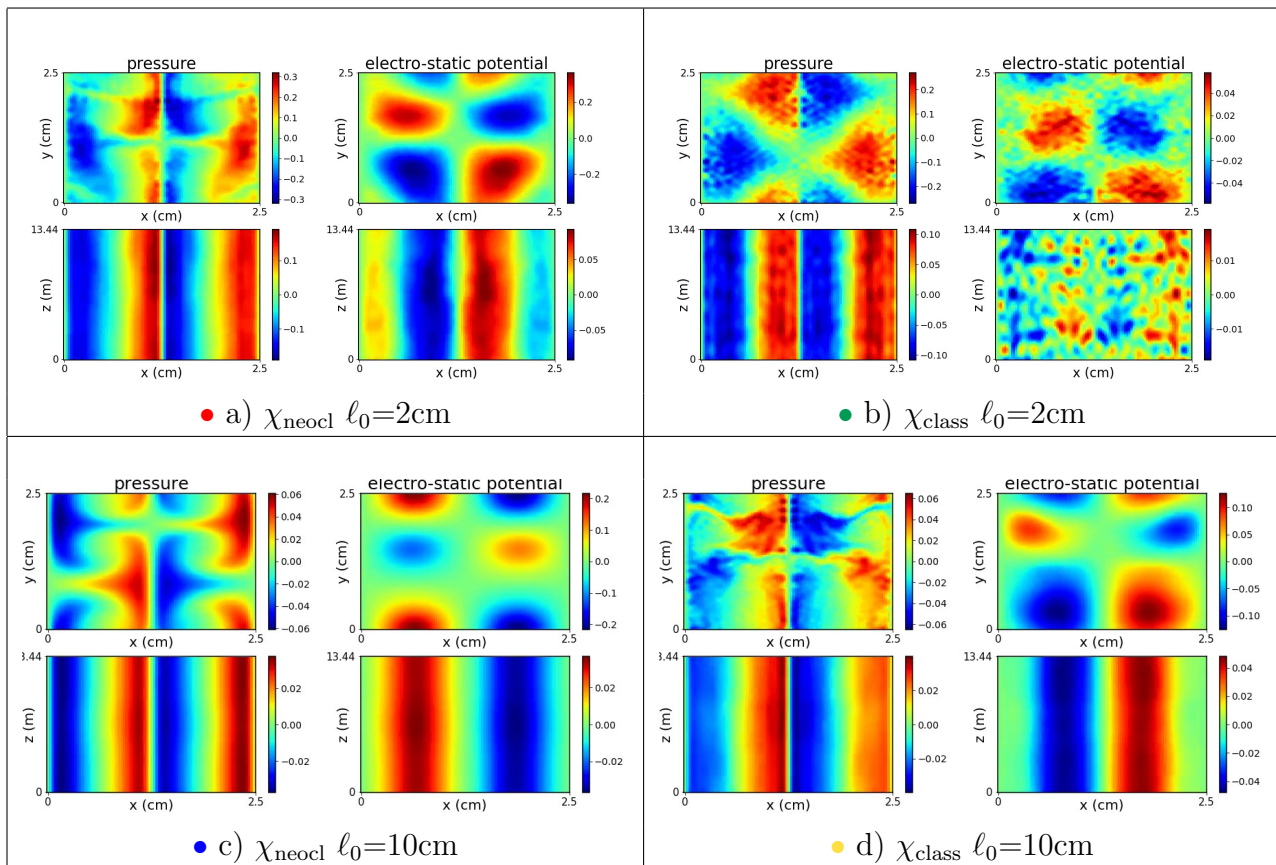


Table 2. The simulation results at time $t = 0.167\text{ms}$ in SLAB for vanishing radial Dirichlet BC. In each panel the figures above contain the poloidal sections, (x, y) plane, of normalized \tilde{p} (left) and ϕ (right) while the figures below are for the radial-toroidal (x, z) plane. The corresponding colorbars are shown next to each plot.

the multi-panel figure Tab.2. The physical solution corresponds to the profiles in the first half of x-axis and the second half just contains a specular copy.

The degree of toroidal symmetry outlines the same qualitative behavior as in the case with fully periodic BC: the most symmetric configuration is obtained in case c) (left bottom panel), with increasing asymmetries while increasing background pressure gradients (bottom to top) and/or reducing diffusivity (left to right). One can also notice the formation of elongated structures in y direction mostly for \tilde{p} .

The ratio of $n = 0$ (solid lines) and $n = m = 0$ (dash-dotted lines) mode amplitudes to the total amplitude is plotted in time in fig.8. The solid lines for \tilde{p} (left) are all close to one, signaling that $n \neq 0$ modes are generically suppressed and except in case b) (green) the dashed lines are quite high, more than 50%, meaning that the saturated modes are mostly poloidally symmetric too. For ϕ (right) one still get strong degree of toroidal symmetry in all cases but b) (green) while the degree of poloidal symmetry is much lower than that for \tilde{p} .

The emergence of elongated structures in y direction is confirmed by the enhancement of the energy spectra for the poloidally symmetric $m = 0$ modes,

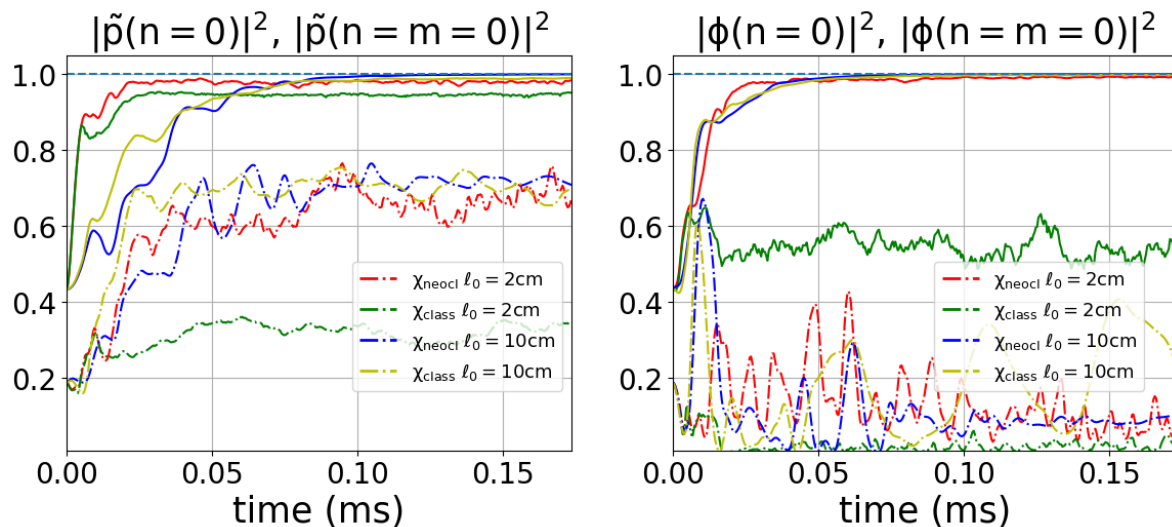


Figure 8. The ratio of $n = 0$ (solid lines) and of $n = m = 0$ (dash-dotted lines) mode amplitudes over the total amplitude for \tilde{p} (left) and ϕ (right) vs time (in ms) for the four considered cases in SLAB with vanishing radial Dirichlet BC.

emphasized graphically by black edges, in Fig.9. Generically, the spectra are mildly anisotropic, especially $E_{\tilde{p}}$ one, and a part from that they are quite similar to those with fully periodic BC (see the dark red and dark yellow lines in Fig.9 reproducing the spectra in Fig.4 for cases a) and d)), except in case b) (green) in which E_{ϕ} is almost constant and $E_{\tilde{p}}$ goes approximately as $1/k_{\perp}$ (left, dark green line).

The toroidal transfer functions $T_{\tilde{p}}^{(n \neq 0 \rightarrow n=0)}$ and $T_{\phi}^{(n \neq 0 \rightarrow n=0)}$ in Fig.10 show a similar qualitative behavior as with fully periodic BC: $T_{\tilde{p}}^{(n \neq 0 \rightarrow n=0)}$ is still negative even if less intense at least for the cases a) (red) and d) (yellow) with respect to the those in fig.5, $T_{\phi}^{(n \neq 0 \rightarrow n=0)}$ is positive/negative for short/long wavelengths, respectively. Moreover, the comparison of the dashed lines (left) with those in fig.5 shows that the flux due to background pressure gradient is generically lower that with fully periodic BC.

2D transfer functions are shown in fig.11. Their magnitude and that of toroidal transitions are of the same order, while the resulting spectral features are highly non trivial and anticorrelated.

Case c) is now a real 2D effective model since toroidal transitions are negligible. This can be seen noting that the values of $T_{\tilde{p}}^{(n \neq 0 \rightarrow n=0)}$ (blue) in Fig.10 are close to zero and lower than their 2D counterparts in Fig.11.

Therefore, the analysis of the simulations in SLAB outlines how there is an effective inverse toroidal cascade, as toroidally symmetric structures develop. However, the magnitude of such cascade is strongly affected by the value of the dissipative (χ_{\perp}) and source (ℓ_0) parameters and non-trivially integrated with 2D transitions leading to various kinds of 2D spectral profiles (that gets wider decreasing diffusivity and increasing background pressure gradients). If vanishing Dirichlet BC are imposed a mild poloidal cascade is also produced leading to the enhancement of poloidally symmetric $m = 0$

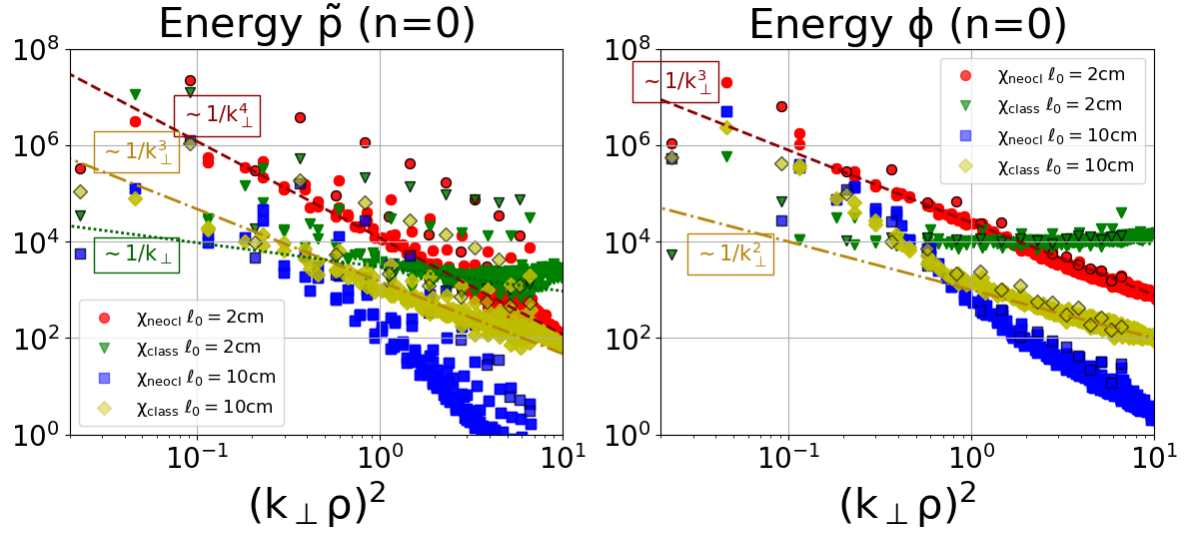


Figure 9. The scatter plots of normalized axisymmetric spectral energies $E_{\tilde{p}}$ (left) and E_{ϕ} (right) vs $(k_{\perp}\rho)^2$ for the four considered cases in SLAB with vanishing radial Dirichlet BC. They are computed by averaging over a time window of $\sim 0.13ms$. Black edges are for those points corresponding to $m = 0$ modes ($k_y = 0$). Some curves are also plotted that approximate quite well some of the spectra profiles and which behave as: $1/k_{\perp}^4$ (dashed dark red line), $1/k_{\perp}^3$ (dash-dotted dark yellow line) and $1/k_{\perp}$ (dotted dark green line) for $E_{\tilde{p}}$ (left) and $1/k_{\perp}^3$ (dashed dark red line) and $1/k_{\perp}^2$ (dash-dotted dark yellow line) for E_{ϕ} (right).

modes and the reduction of turbulence free-energy source.

3.2. Constant poloidal field

We consider now a constant poloidal field, characterized by $B_x = 0$ and

$$\frac{B_y}{B_z} = \alpha \quad (15)$$

and the constant parameter $\alpha = \frac{L_{\perp}}{L_{\parallel}} = 1.5 \cdot 10^{-3}$ is chosen such that in normalized coordinates the parallel direction is diagonal in (y, z) plane. This choice corresponds to a very large safety factor $q \sim 700$ and it is a reliable model for the SOL region far from the X-point (limiter-like configuration of the tokamak). The projection of x and y derivatives onto the perpendicular plane are $\delta_x = \partial_x$ and $\delta_y = \partial_y + \hat{b}_y \frac{L_{\perp}}{L_{\parallel}} \partial_z \sim \partial_y$ and the perpendicular Laplacian operator in FS reads

$$\Delta_{\perp} = k_x^2 + \frac{1}{1 + \hat{b}_y^2} \left(k_y - \hat{b}_y \frac{L_{\perp}}{L_{\parallel}} k_z \right)^2 \sim k_x^2 + k_y^2 \quad (16)$$

that is close to the expression in SLAB. The main modification is the expression of the parallel derivative that now reads

$$\nabla_{\parallel} = \frac{1}{\sqrt{1 + \hat{b}_y^2}} \left(k_z + \hat{b}_y \frac{L_{\parallel}}{L_{\perp}} k_z \right) \quad (17)$$

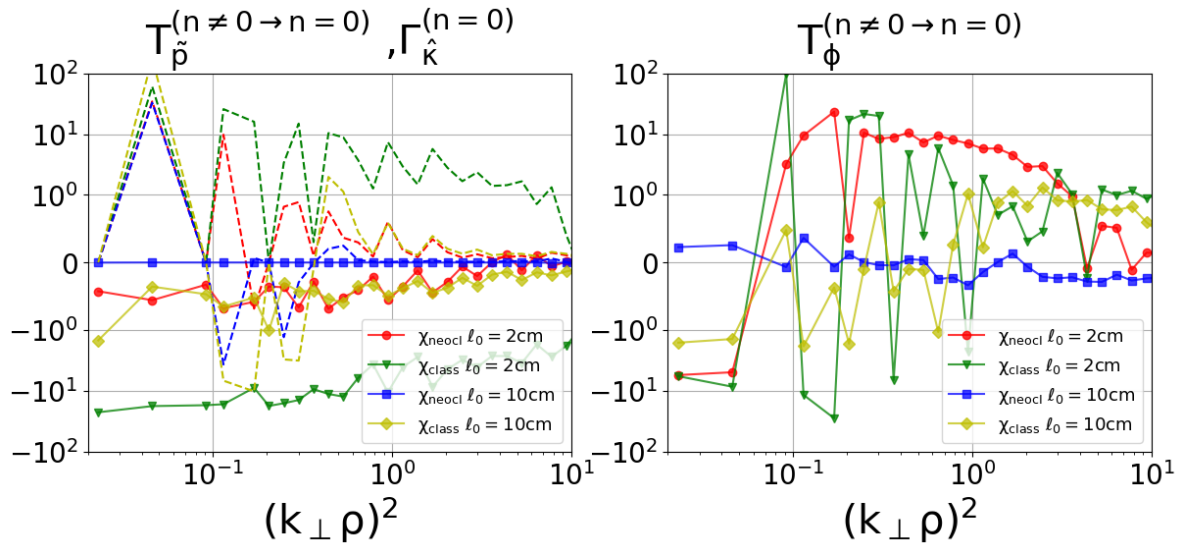


Figure 10. The nonlinear transfer functions of toroidal transitions $n \neq 0 \rightarrow n = 0$ (solid lines) for \tilde{p} (left) and ϕ (right) vs $(k_{\perp}\rho)^2$ and the flux due to background pressure gradient (dashed lines, left) for the four considered cases in SLAB with vanishing radial Dirichlet BC. Each plotted value is normalized with the corresponding dissipative flux, *i.e.* the diffusivity and the viscous contributions for \tilde{p} and ϕ , respectively. The chosen values of $(k_{\perp}\rho)^2$ are constructed from the computational Cartesian grid in FS by taking the five smallest values of k_{\perp} and by logarithmically sampling the relic part.

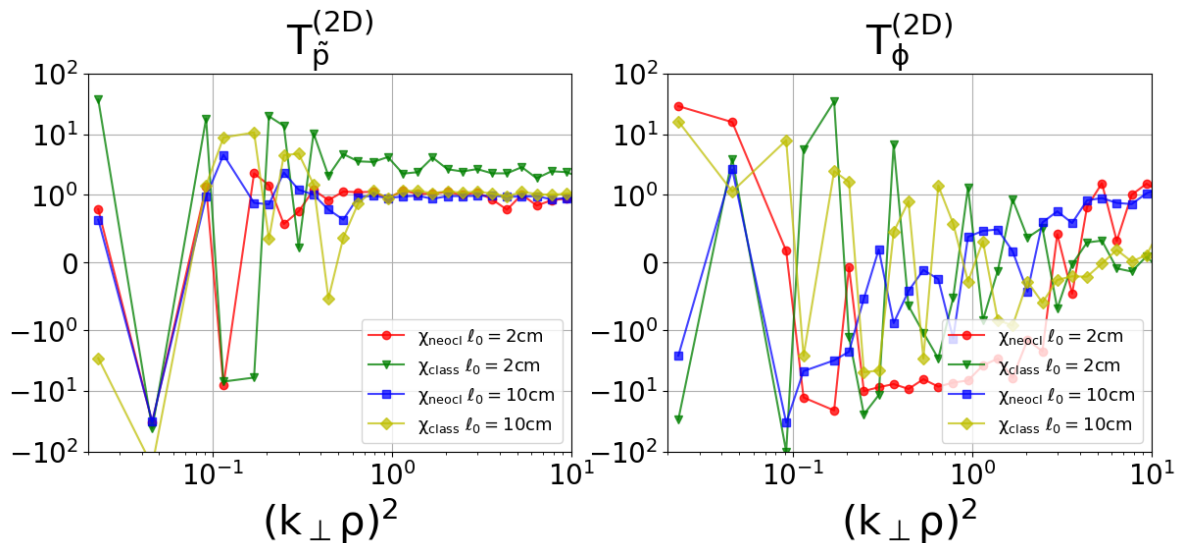


Figure 11. The nonlinear transfer functions of 2D transitions $n = 0 \rightarrow n = 0$ (solid lines) for \tilde{p} (left) and ϕ (right) vs $(k_{\perp}\rho)^2$ for the four considered cases in SLAB with vanishing radial Dirichlet BC. Each plotted value is normalized with the corresponding dissipative flux, *i.e.* the diffusivity and the viscous contributions for \tilde{p} and ϕ , respectively.

and it depends on y derivatives explicitly breaking isotropy in the poloidal plane.

The results of the simulations are shown in the multi-panel figure Tab.3.

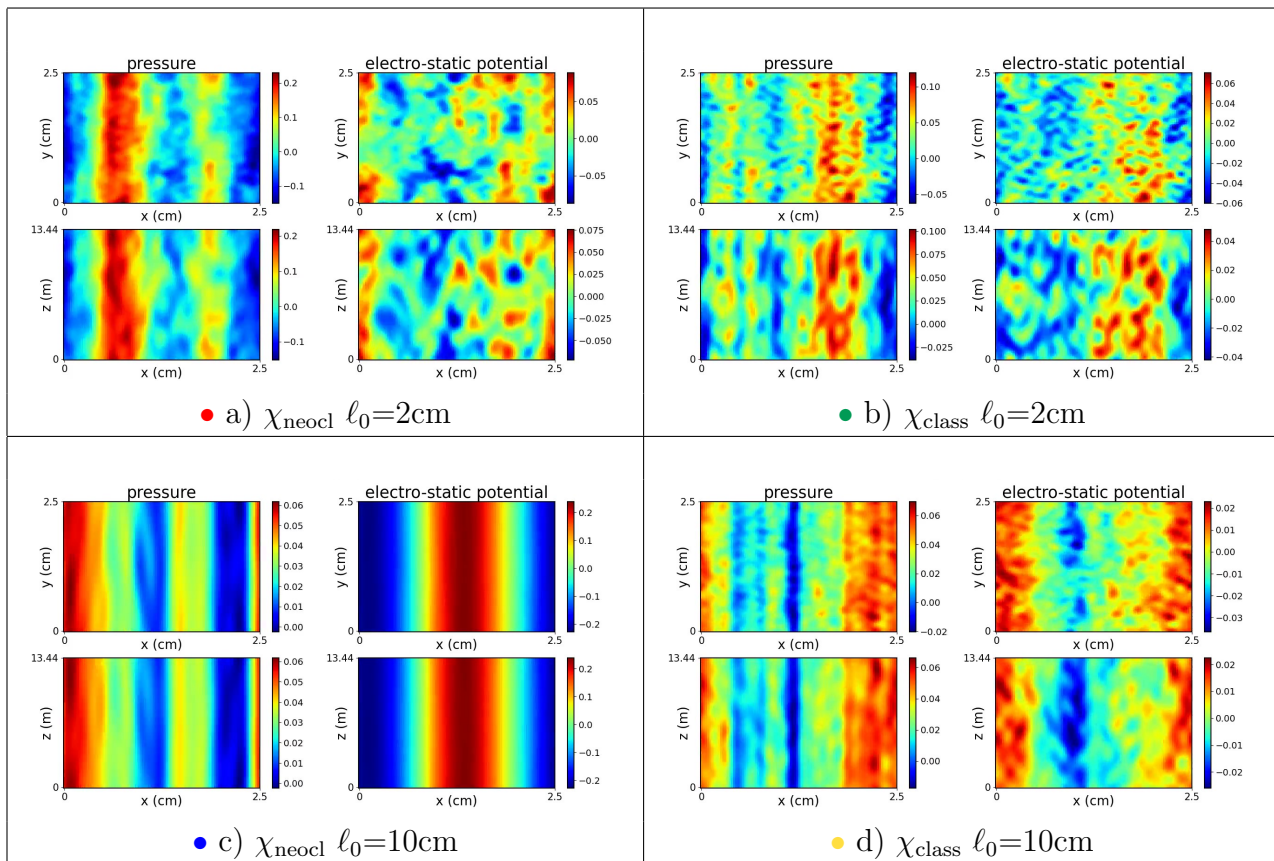


Table 3. The simulation results at time $t = 0.167ms$ for constant poloidal magnetic field and fully periodic BC. In each panel the figures above contain the poloidal sections, (x, y) plane, of normalized \tilde{p} (left) and ϕ (right) while the figures below are for the radial-toroidal (x, z) plane. The corresponding colorbars are shown next to each plot.

One can notice the emergence of configurations with a similar degree of homogeneity along both z and y directions, with cases c) (left bottom panel) and b) (right top panel) being the most and least symmetric ones, respectively. In other words, the inverse toroidal cascade typical of SLAB case here proceeds in conjunction with a similar cascade along the poloidal direction y . This is confirmed by:

- the plots of the fraction of $n = 0$ (solid lines) and $n = m = 0$ (dash-dotted lines) mode amplitudes in Fig.12, that overlap in all cases except b) (green), where the latter is slightly lower than the former, signaling that most of the amplitude of toroidally symmetric mode is also poloidally symmetric,
- the 2D spectra in Fig.13, that show the anisotropy in (k_x, k_y) plane with leading poloidally symmetric $m = 0$ modes (outlined with black edges).

The spectral energy values are now more scattered at given k_{\perp} with respect to SLAB (see also the reference red, green and yellow curves in Fig.13 that helps the comparison with the spectra in Figs.4 and 9), signaling strong anisotropy. Therefore the spectra are now quite different from those in SLAB, outlining how the modification of the drift terms according to Eq.(17) has a strong impact on the resulting spectral features.

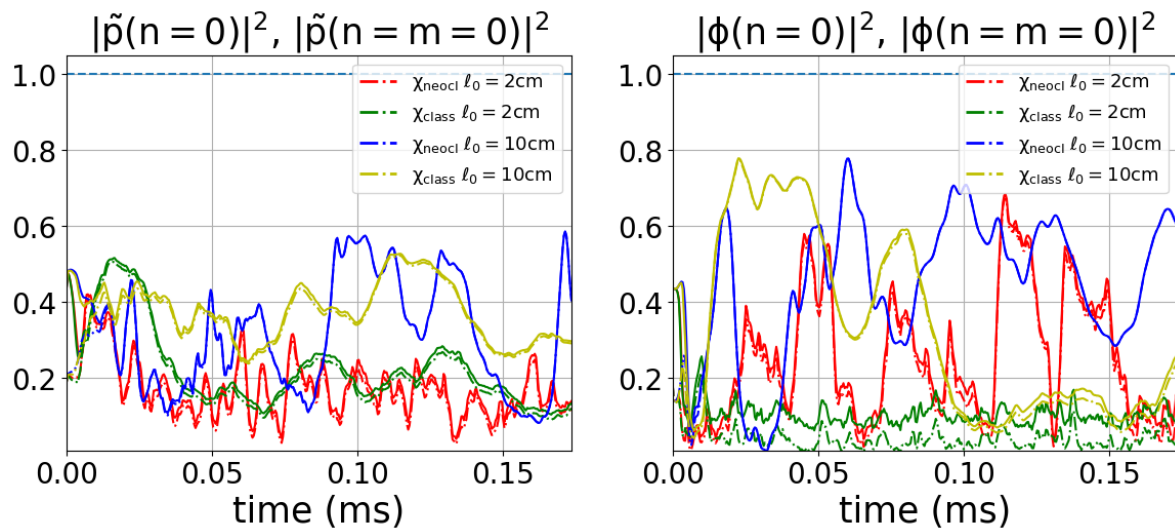


Figure 12. The ratio of $n = 0$ (solid lines) and of $n = m = 0$ (dash-dotted lines) mode amplitudes over the total amplitude for \tilde{p} (left) and ϕ (right) vs time (in ms) for the four considered cases with constant poloidal magnetic field and fully periodic BC.

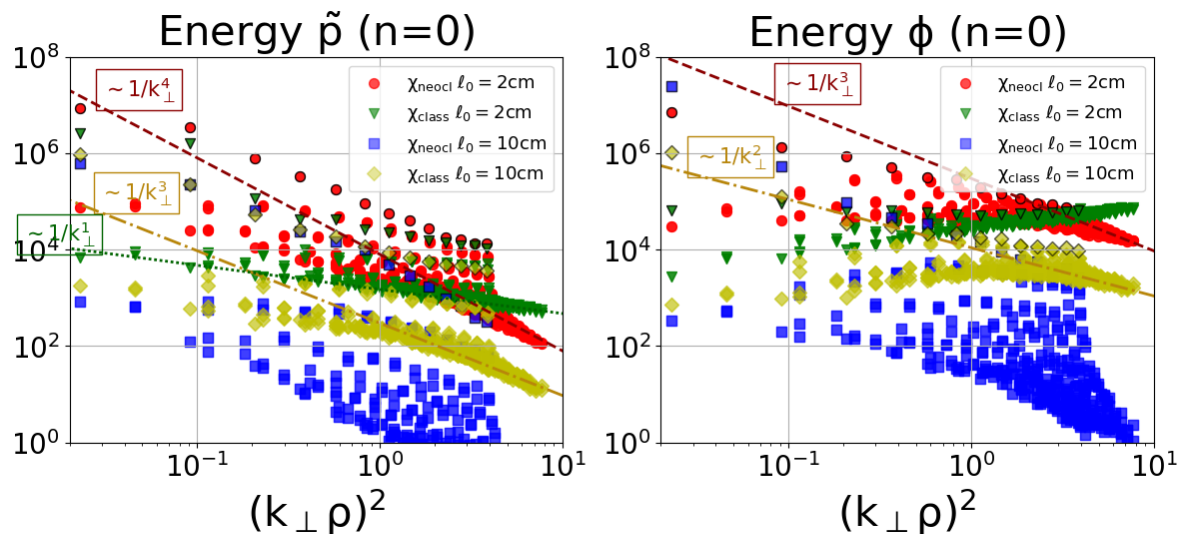


Figure 13. The scatter plots of normalized axisymmetric spectral energies $E_{\tilde{p}}$ (left) and E_{ϕ} (right) vs $(k_{\perp}\rho)^2$ for the four considered cases with constant poloidal magnetic field and fully periodic BC. They are computed by averaging over a time window of $\sim 0.13ms$. Black edges are for those points corresponding to $m = 0$ modes ($k_y = 0$). For reference some curves are also plotted that approximate quite well some of the spectra profiles in SLAB (see Figs.4 and 9) and which behave as: $1/k_{\perp}^4$ (dashed dark red line), $1/k_{\perp}^3$ (dash-dotted dark yellow line) and $1/k_{\perp}$ (dotted dark green line) for $E_{\tilde{p}}$ (left) and $1/k_{\perp}^3$ (dashed dark red line) and $1/k_{\perp}^2$ (dash-dotted dark yellow line) for E_{ϕ} (right).

Toroidal transition functions are plotted for logarithmically sampled k_{\perp} values in Figs.14.

It is worth noting how $T_{\tilde{p}}^{(n \neq 0 \rightarrow n=0)}$ (left) are mostly positive, signaling an inverse

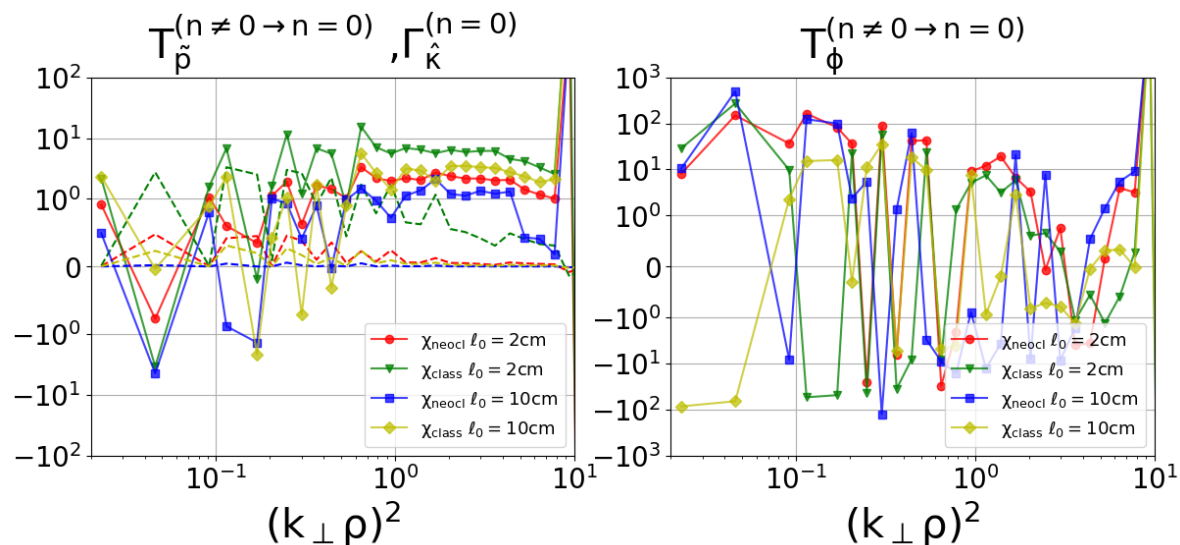


Figure 14. The nonlinear transfer functions of toroidal transitions $n \neq 0 \rightarrow n = 0$ (solid lines) for \tilde{p} (left) and ϕ (right) vs $(k_{\perp}\rho)^2$ and the flux due to background pressure gradient (dashed lines, left) for the four considered cases with constant poloidal magnetic field and fully periodic BC. Each plotted value is normalized with the corresponding dissipative flux, *i.e.* the diffusivity and the viscous contributions for \tilde{p} and ϕ , respectively. The chosen values of $(k_{\perp}\rho)^2$ are constructed from the computational Cartesian grid in FS by taking the five smallest values of k_{\perp} and by logarithmically sampling the relic part.

toroidal cascade for \tilde{p} . Moreover, except for the largest wave-lengths ($(k_{\perp}\rho)^2 < 10^{-1}$), it is the leading source contribution with larger magnitude with respect to both $\Gamma_{\hat{k}}$ (dashed curves) and $T_{\cdot}^{(n=0)}(2D)$ in Fig.15 and it compensated by the drift term in Fig.16 (left).

The interplay between toroidal and 2D transitions and the drift term is less clear for ϕ , with $T_{\phi}^{(2D)}$ sub-dominant with respect to the to other contributions for short wave-length $(k_{\perp}\rho) > 1$.

Case c) (blue) still exhibits the same kind of turbulence reduction in time shown in SLAB. In particular, a stationary sheared radial electric field develops (see Fig.17) with averaged value close to $l = 1$ mode and small variations along poloidal and toroidal directions (small shaded region).

3.2.1. Dirichlet BC The simulation results with constant poloidal field and vanishing radial Dirichlet BC are shown in multi-panel figure Tab.4.

The specularity of \tilde{p} and ϕ profiles along x signals that the BC have been implemented correctly. The formation of more or less symmetric profiles along y and z depending on the considered case (c) the most symmetric, b) the least symmetric ones) is analogous to the results with fully periodic BC. The spectral anisotropy, that in SLAB resulted from the implementation of vanishing radial Dirichlet BC, sums up to that due to the poloidal drift component. In fact, the resulting energy spectra in Fig.18 present even more anisotropy with respect to those in Fig.13, especially one can notice a major

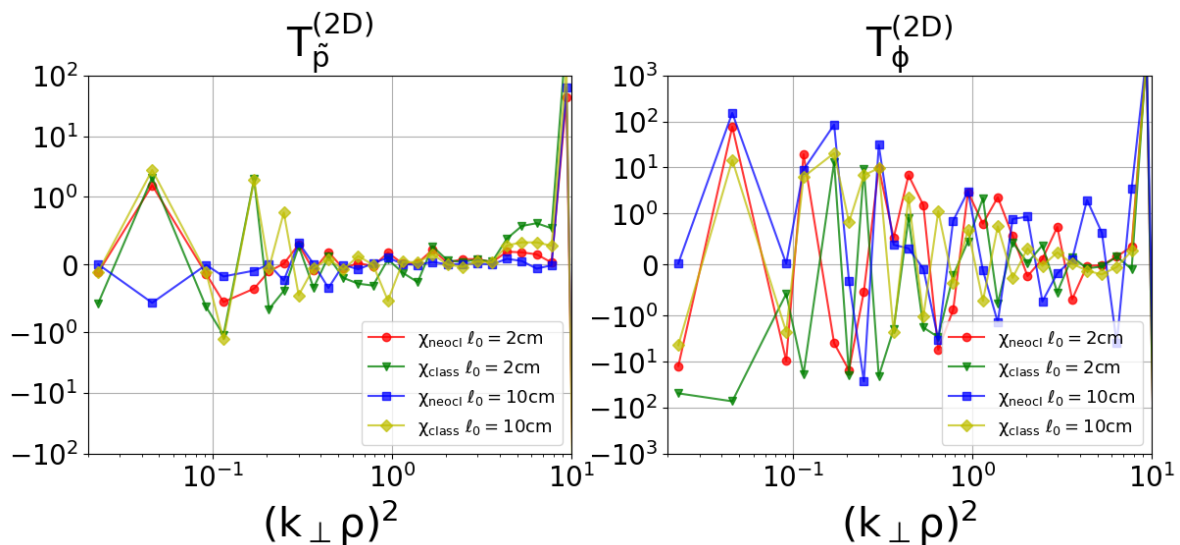


Figure 15. The nonlinear transfer functions of 2D transitions $n = 0 \rightarrow n = 0$ (solid lines) for \tilde{p} (left) and ϕ (right) vs $(k_{\perp}\rho)^2$ for the four considered cases with constant poloidal magnetic field and fully periodic BC. Each plotted value is normalized with the corresponding dissipative flux, *i.e.* the diffusivity and the viscous contributions for \tilde{p} and ϕ , respectively.

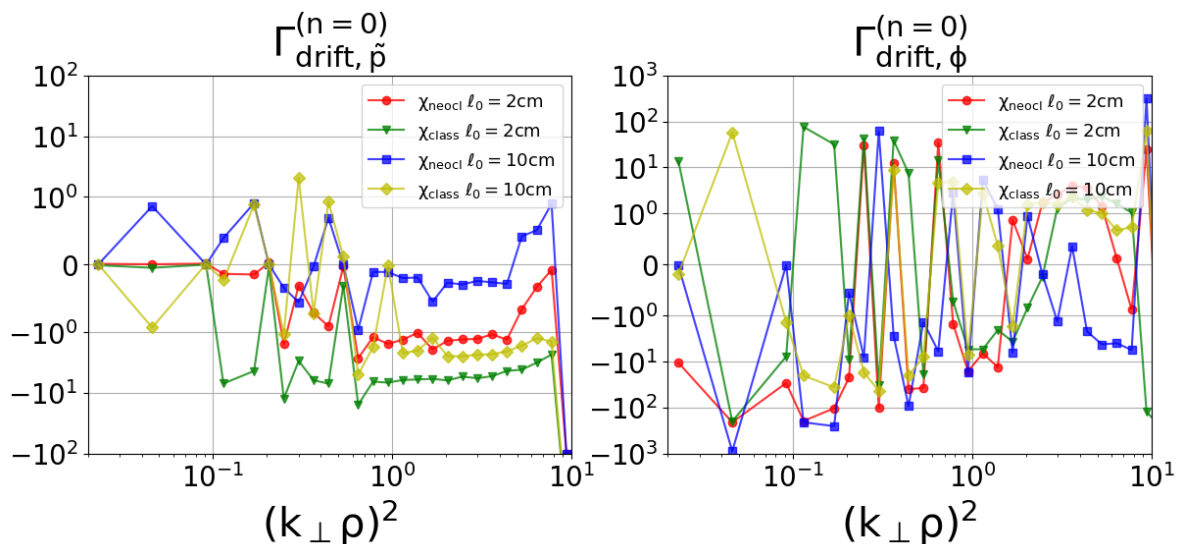


Figure 16. The fluxes due to the drift coupling (solid lines) for \tilde{p} (left) and ϕ (right) vs $(k_{\perp}\rho)^2$ for the four considered cases with constant poloidal magnetic field and fully periodic BC. Each plotted value is normalized with the corresponding dissipative flux, *i.e.* the diffusivity and the viscous contributions for \tilde{p} and ϕ , respectively.

enhancement of $m = 0$ modes for \tilde{p} .

The analysis of 3D and 2D transitions and of the drift terms provide similar qualitative results as in the case of fully periodic BC, with inverse toroidal cascade for \tilde{p} and negligible 2D transitions at long wave-lengths for ϕ . Case c) (blue) still shows turbulence reduction in time and the formation of a stationary radial electric field.

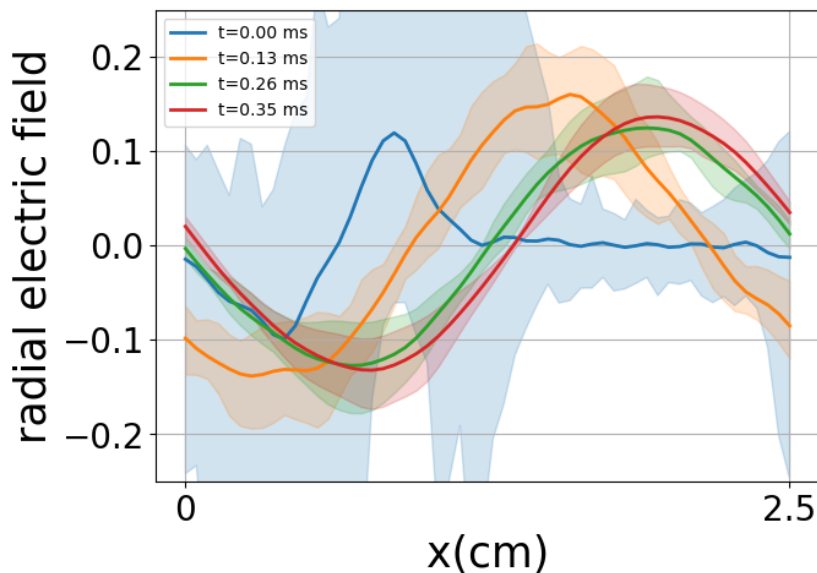


Figure 17. The profile of the radial electric field in case c) with constant poloidal magnetic field and fully periodic BC at four given time values: start (blue), $t = 0.04ms$ (orange), $t = 0.09ms$ (green) and $t = 0.17ms$ (red). The solid lines denote the averaged value along y and z directions, while the corresponding shaded regions cover the whole range of variability along such directions at the given time values.

Therefore, the simulations with constant poloidal magnetic field outline how the introduction of a poloidal magnetic field component provides an inverse poloidal cascade in addition to the toroidal one already seen in SLAB. This fact suggests that the direction of the inverse cascade in FS is determined by that of the drift term. The resulting 2D spectra are anisotropic with leading poloidally symmetric modes and their profiles are affected by the value of the dissipative (χ_{\perp}) and source (ℓ_0) parameters similarly to SLAB case, *i.e* they get wider by reducing χ_{\perp} and/or ℓ_0 .

3.3. Radial magnetic shear

A radially sheared poloidal field is discussed in this section, with magnetic components $B_x = 0$ and B_y ranging from SLAB case at the midpoint $l_x/2$ of the radial simulation domain $[0, l_x]$ to \pm the constant poloidal field discussed in the previous section at the borders $x = 0$ and $x = l_x$. The chosen form is

$$B_y = B_z \frac{2\alpha}{l_x} \left(x - \frac{l_x}{2} \right) \quad (18)$$

with the parameter $\alpha = \frac{L_{\perp}}{L_{\parallel}} = 1.5 \cdot 10^{-3}$. The expressions of Δ_{\perp} and ∇_{\parallel} are formally the same as in the case with constant poloidal field, Eqs.(16) and (17), respectively, but since \hat{b}_y is now a function of x radial coordinate the corresponding expressions are not anymore multiplicative operators in FS and are numerically computed with the pseudospectral method.

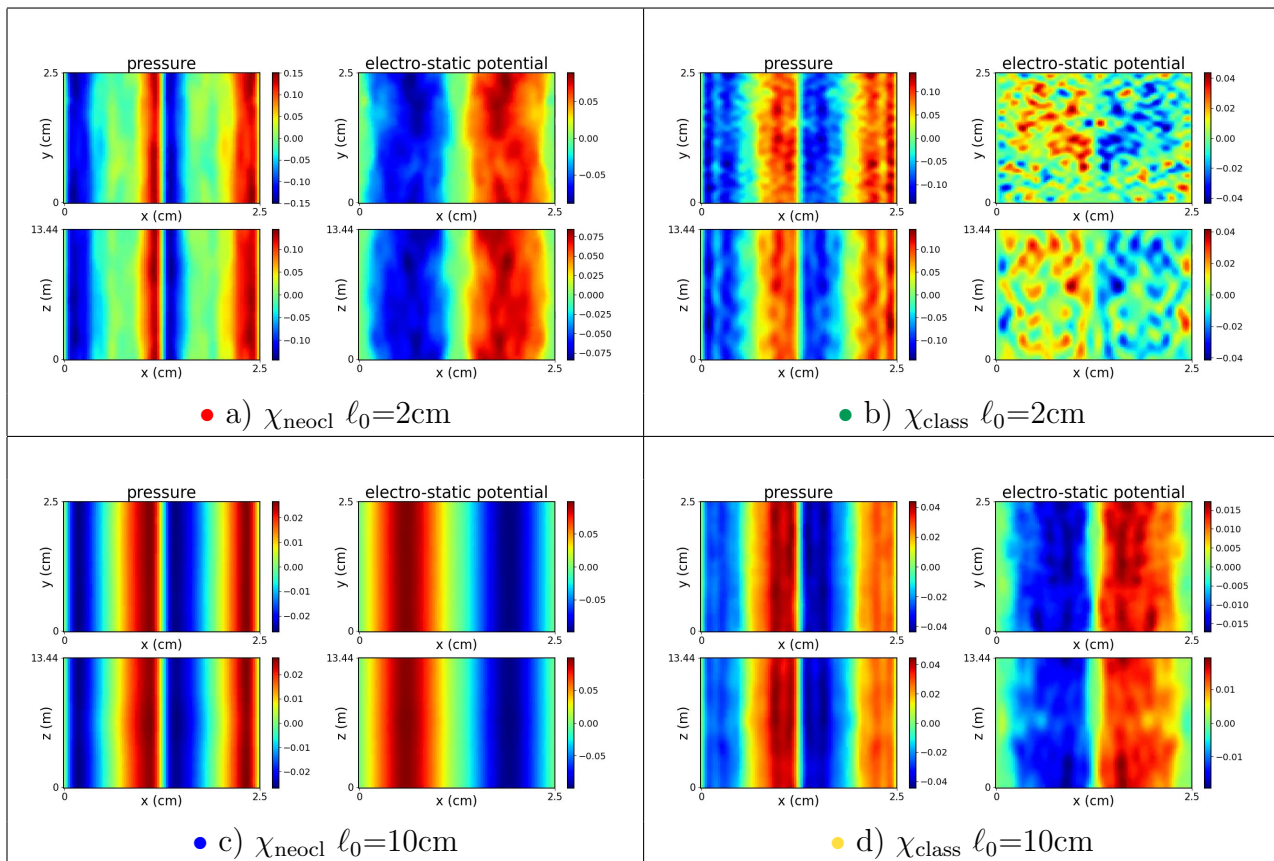


Table 4. The simulation results at time $t = 0.167ms$ for constant poloidal magnetic field and vanishing radial Dirichlet BC. In each panel the figures above contains the poloidal sections, (x, y) plane, of \tilde{p} (left) and ϕ (right) while the figures below are for the radial-toroidal (x, z) plane. The corresponding colorbars are shown next to each plot.

The magnetic shear is known to stabilize turbulence and this is confirmed by the simulations shown in the multi-panel figure Tab.5, which generically exhibit weaker turbulence amplitude with respect to the analogous results in the two other considered magnetic configurations (shown in the multi-panel figures Tabs.1 and 3).

The fraction of $n = 0$ (solid lines) and $n = m = 0$ (dash-dotted lines) mode amplitudes are plotted in Fig.19. The solid lines for \tilde{p} approach ~ 0.8 for cases a) and b) (red and green), ~ 0.9 for case d) (yellow) and ~ 1 for c) (blue), while the same curves for ϕ reach 1 in the two neoclassical cases a) and c) (red and blue), ~ 0.75 for d) (yellow) and 0.2 for b) (green). The dash-dotted lines are slightly lower than solid ones, meaning that most of the toroidally symmetric modes are poloidally symmetric too. Therefore, we get a similar cascade along y as for a constant poloidal field (see Fig.12), while the toroidal cascade more resembles the SLAB profile (see Fig.3).

The energy spectra are shown in Fig.20 and they exhibit intermediate properties between the magnetic configurations previously discussed: a similar degree of anisotropy as for constant poloidal magnetic field in Fig.13 and an averaged profile that roughly follows the reference curves reproducing the behavior in SLAB .

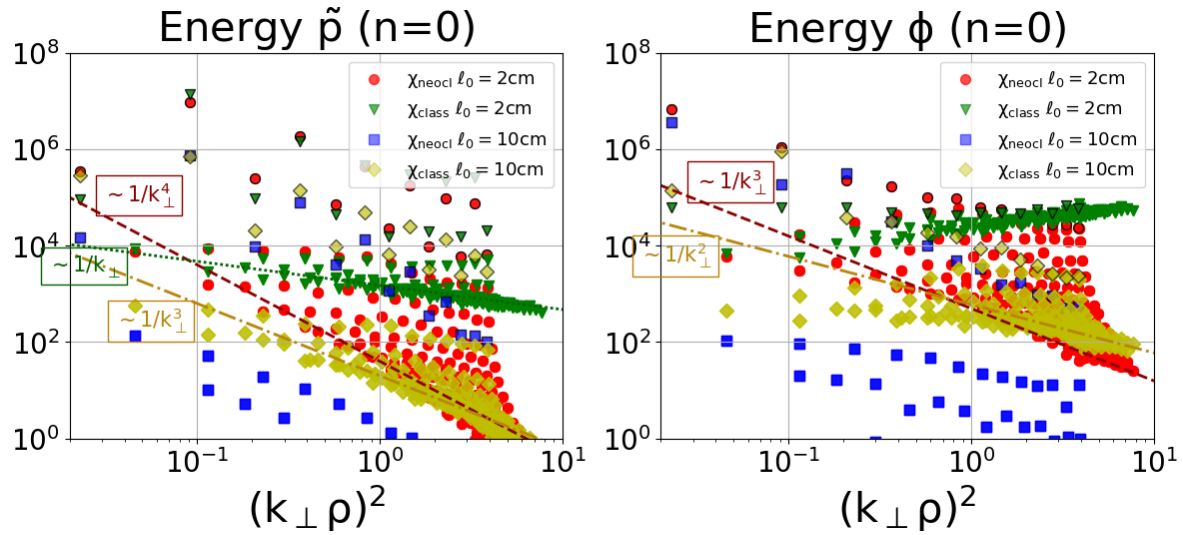


Figure 18. The scatter plots of normalized axisymmetric spectral energies $E_{\tilde{p}}$ (left) and E_{ϕ} (right) vs $(k_{\perp}\rho)^2$ for the four considered cases with constant poloidal magnetic field and vanishing radial Dirichlet BC. They are computed by averaging over a time window of $\sim 0.13ms$. Black edges are for those points corresponding to $m = 0$ modes ($k_y = 0$). For reference some curves are also plotted that approximate quite well some of the spectra profiles in SLAB (see Figs.4 and 9) and which behave as: $1/k_{\perp}^4$ (dashed dark red line), $1/k_{\perp}^3$ (dash-dotted dark yellow line) and $1/k_{\perp}$ (dotted dark green line) for $E_{\tilde{p}}$ (left) and $1/k_{\perp}^3$ (dashed dark red line) and $1/k_{\perp}^2$ (dash-dotted dark yellow line) for E_{ϕ} (right).

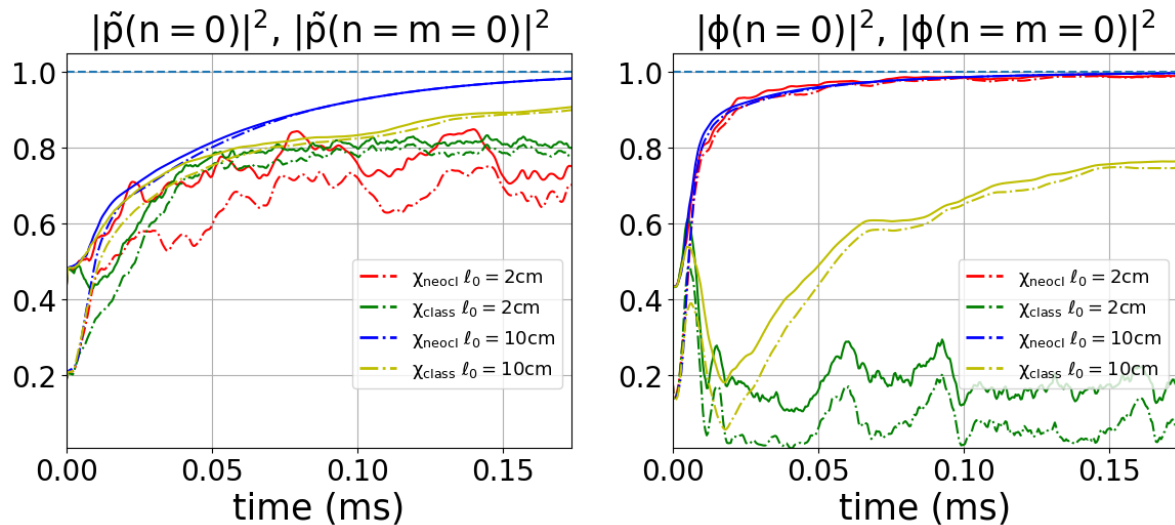


Figure 19. The ratio of $n = 0$ (solid lines) and of $n = m = 0$ (dash-dotted lines) mode amplitudes over the total amplitude for \tilde{p} (left) and ϕ (right) vs time (in ms) for the four considered cases with radially sheared poloidal magnetic field and fully periodic BC.

Toroidal transfer functions for \tilde{p} in Fig.21 (left) have a sort of mixed behavior: there is a direct toroidal cascade at short wave-lengths as in SLAB and an inverse one at long

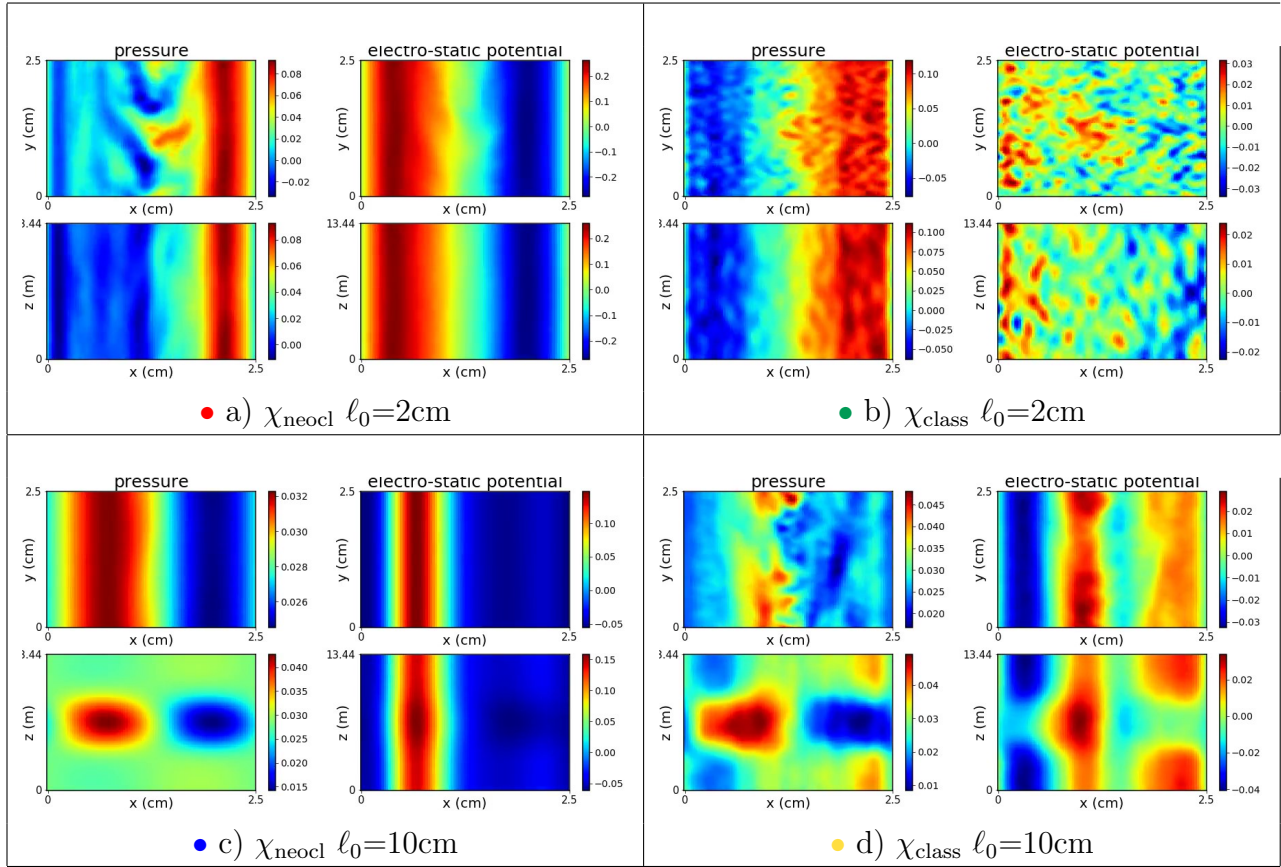


Table 5. The simulation results at time $t = 0.167\text{ms}$ for radially sheared poloidal magnetic field and fully periodic BC. In each panel the figures above contain the poloidal sections, (x, y) plane, of normalized \tilde{p} (left) and ϕ (right) while the figures below for the radial-toroidal (x, z) plane. The corresponding colorbars are shown next to each plot.

wave-lengths as for the constant poloidal field. These quantities are very close to zero in the two neoclassical cases a) and c) (red and blue) which correspond to toroidal and poloidal symmetry (this can be seen in both Figs.5 and 19).

The toroidal transfer functions for ϕ (right) have strong fluctuations for neighbor sampled $(k_{\perp}\rho)^2$ values and they strongly depend from case to case. Their magnitude are comparable to those of 2D transitions in Fig.22.

Finally, the drift fluxes are shown in Fig.23 and they outline similar features as for a constant poloidal field: they are mostly sink contributions for \tilde{p} (negative), while no definite behavior is seen for ϕ . In all cases, they have a similar magnitude as toroidal and 2D transitions.

The conclusion of fluxes analysis is that spectral profiles are determined by the combination of both 2D and toroidal transitions with the linear contributions, *i.e.* those due to background pressure gradient for \tilde{p} , drift terms and dissipation.

Like in the other considered magnetic geometries, case c) is peculiar as turbulence gets suppressed in time and a sheared radial electric field is generated as shown in Fig.24.

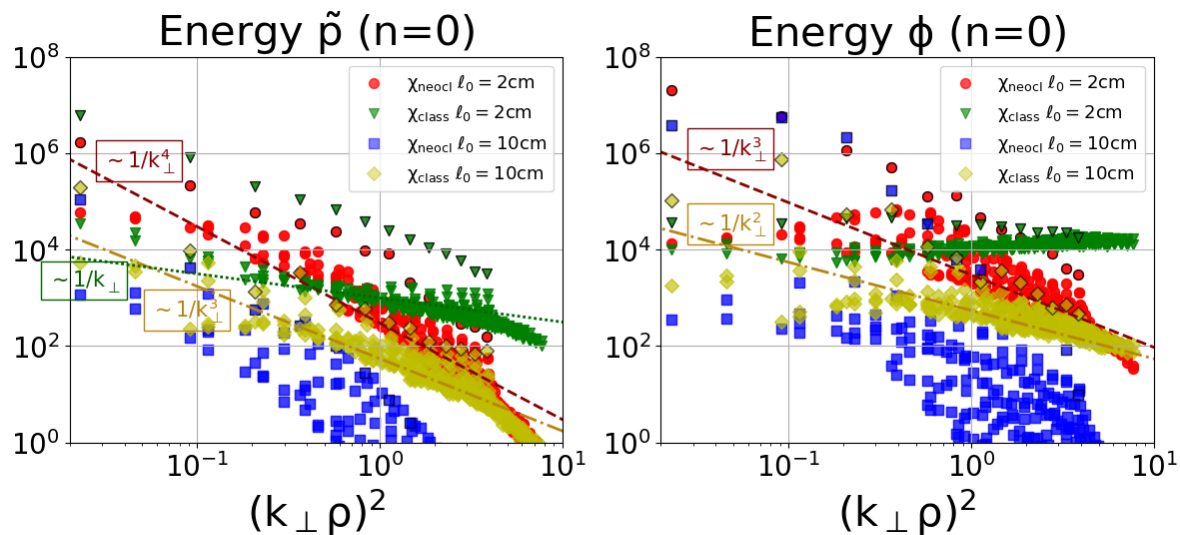


Figure 20. The scatter plots of normalized axisymmetric spectral energies $E_{\tilde{p}}$ (left) and E_{ϕ} (right) vs $(k_{\perp}\rho)^2$ for the four considered cases with radially sheared poloidal magnetic field and fully periodic BC. They are computed by averaging over a time window of $\sim 0.13ms$. Black edges are for those points corresponding to $m = 0$ modes ($k_y = 0$). For reference some curves are also plotted that approximate quite well some of the spectra profiles in SLAB (see Figs.4 and 9) and which behave as: $1/k_{\perp}^4$ (dashed dark red line), $1/k_{\perp}^3$ (dash-dotted dark yellow line) and $1/k_{\perp}$ (dotted dark green line) for $E_{\tilde{p}}$ (left) and $1/k_{\perp}^3$ (dashed dark red line) and $1/k_{\perp}^2$ (dash-dotted dark yellow line) for E_{ϕ} (right).

The profile is toroidally and poloidally symmetric, as the extent of the shaded area is very small since $t = 0.13ms$ (orange) and it is nonvanishing only in the first half of x simulation domain, where the initial wave-packet is localized.

3.3.1. Dirichlet BC The simulation results with the sheared magnetic geometry in Eq.(18) and vanishing radial Dirichlet BC are shown in the multi-panel figure Tab.6.

It is worth noting how poloidally symmetric and, to a minor extent, toroidally symmetric configurations develop in ϕ , especially in cases a), c) and d), while the pressure profiles keep a certain degree of asymmetry in both directions in all cases. This is confirmed by the plots in Fig.25 of the fraction of $n = 0$ (solid lines) and $n = m = 0$ modes (dash-dotted lines). For ϕ (right), in all cases except b) (blue) the solid and dot-dashed lines overlap and reach values close to one, signaling that both poloidally and toroidally symmetric configurations are obtained. This finding is in qualitative agreement with the case with fully periodic BC (see Fig.25), while in case b) (green) one gets an enhancement of toroidally symmetric mode amplitude by a factor 3 (from 20% in Fig.25 to 60% here).

The same plots for \tilde{p} (left) exhibit much lower degree of symmetry in both directions: the fraction of toroidally symmetric mode amplitude (solid lines) is in the range $40\% \div 60\%$ and except for c) (blue) the fraction of poloidally symmetric modes (dash-

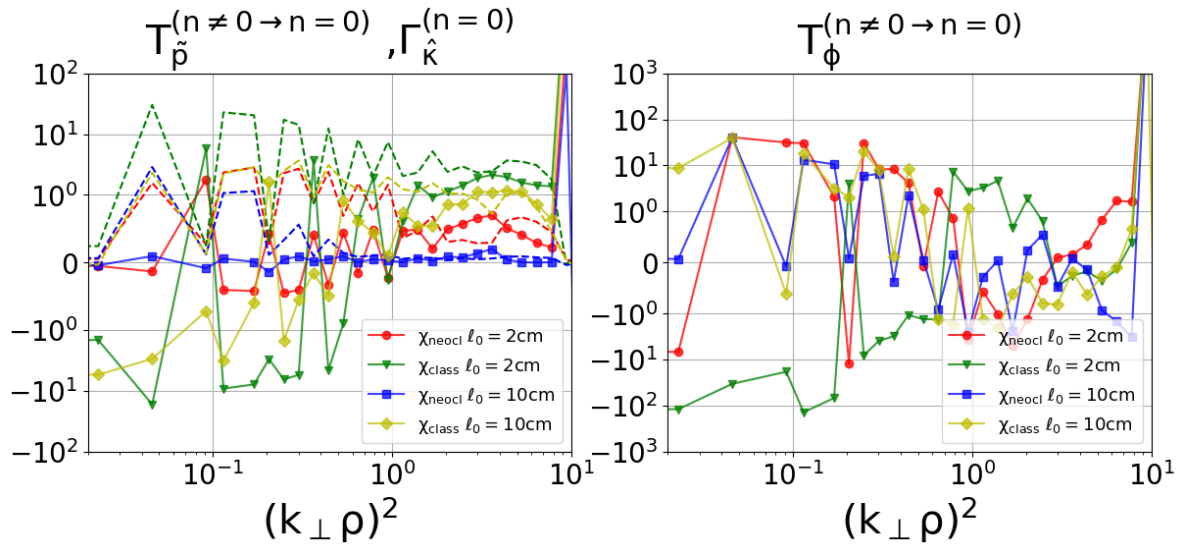


Figure 21. The nonlinear transfer functions of toroidal transitions $n \neq 0 \rightarrow n = 0$ (solid lines) for \tilde{p} (left) and ϕ (right) vs $(k_{\perp}\rho)^2$ and the flux due to background pressure gradient (dashed lines, left) for the four considered cases with radially sheared poloidal magnetic field and fully periodic BC. Each plotted value is normalized with the corresponding dissipative flux, *i.e.* the diffusivity and the viscous contributions for \tilde{p} and ϕ , respectively. The chosen values of $(k_{\perp}\rho)^2$ are constructed from the computational Cartesian grid in FS by taking the five smallest values of k_{\perp} and by logarithmically sampling the relic part.

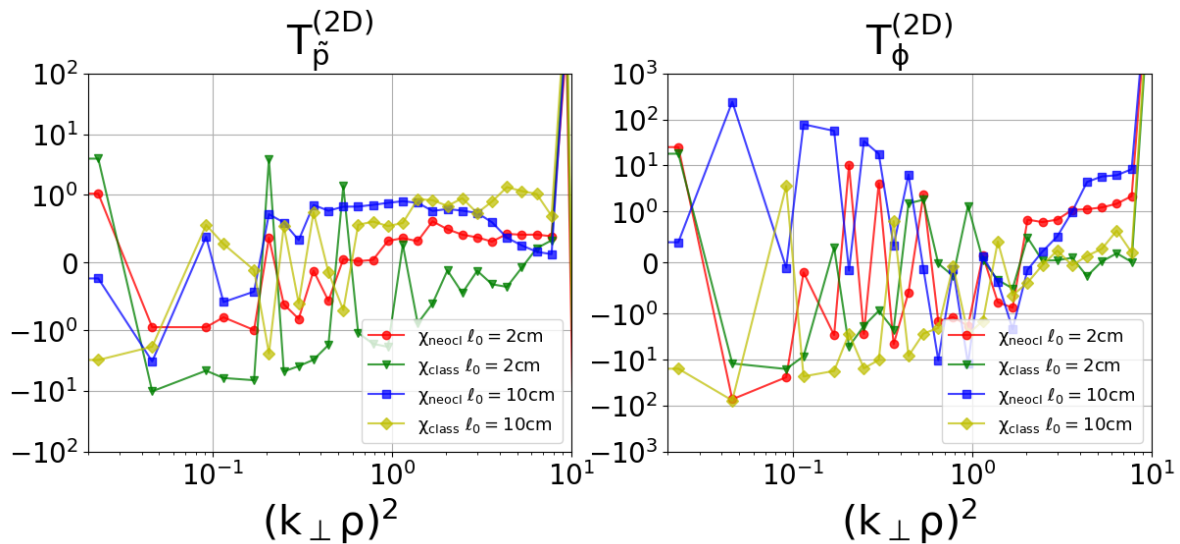


Figure 22. The nonlinear transfer functions of 2D transitions $n = 0 \rightarrow n = 0$ (solid lines) for \tilde{p} (left) and ϕ (right) vs $(k_{\perp}\rho)^2$ for the four considered cases with radially sheared poloidal magnetic field and fully periodic BC. Each plotted value is normalized with the corresponding dissipative flux, *i.e.* the diffusivity and the viscous contributions for \tilde{p} and ϕ , respectively.

dotted lines) is significantly lower.

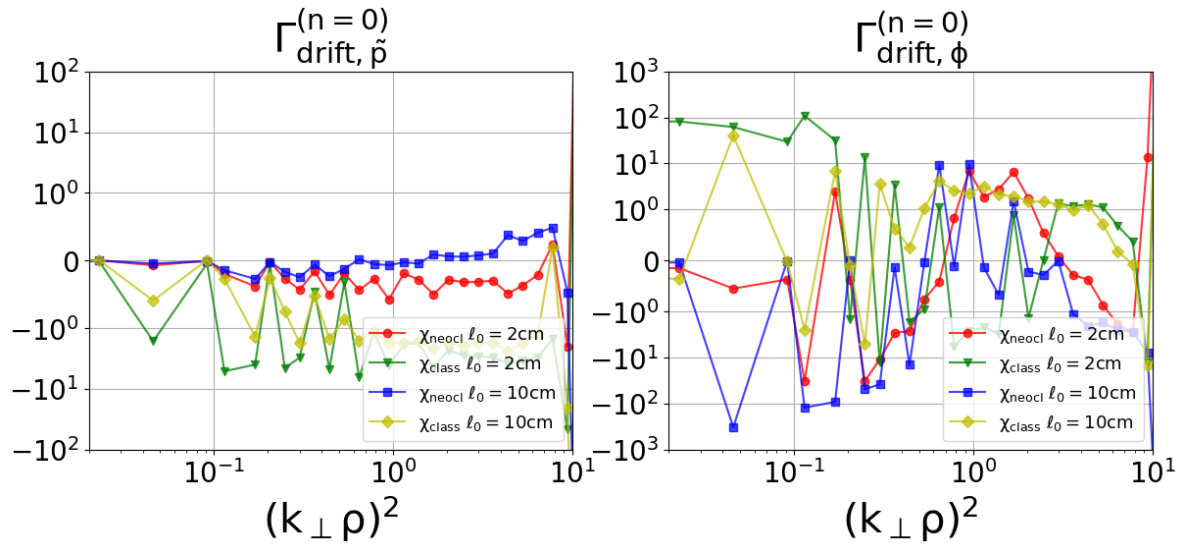


Figure 23. The fluxes due to the drift coupling (solid lines) for \tilde{p} (left) and ϕ (right) vs $(k_{\perp} \rho)^2$ for the four considered cases with radially sheared poloidal magnetic field and fully periodic BC. Each plotted value is normalized with the corresponding dissipative flux, *i.e.* the diffusivity and the viscous contributions for \tilde{p} and ϕ , respectively.

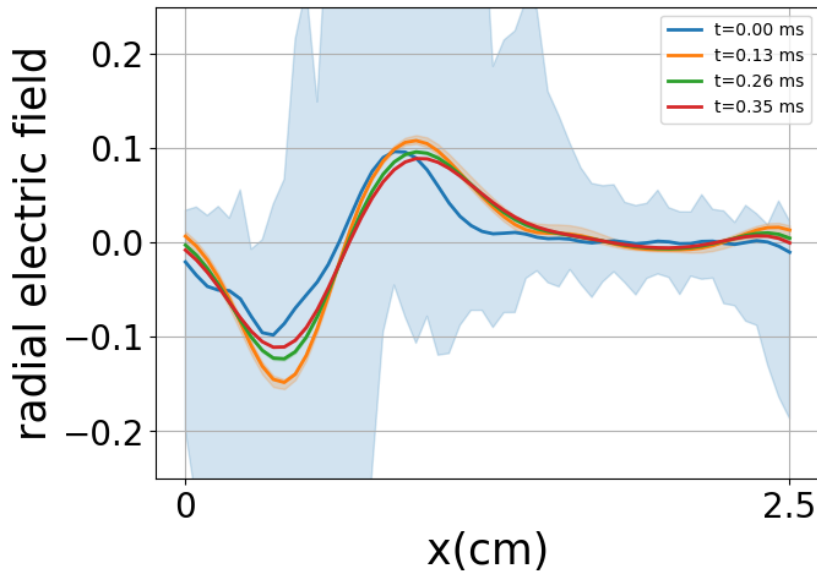


Figure 24. The profile of the radial electric field in case c) with radially sheared poloidal magnetic field and fully periodic BC at four given time values: start (blue), $t = 0.04\text{ms}$ (orange), $t = 0.09\text{ms}$ (green) and $t = 0.17\text{ms}$ (red). The solid lines denote the averaged value along y and z directions, while the corresponding shaded regions cover the whole range of variability along such directions at the given time values.

2D energy spectra are shown in Fig.26 and they have generically similar profiles but stronger anisotropy with respect to those for fully periodic BC in cases a) (red), b) (green) and c) (blue). This can be seen by comparing the amplification of $m = 0$ modes (with black edges) with respect to other modes at same k_{\perp} values, that is here

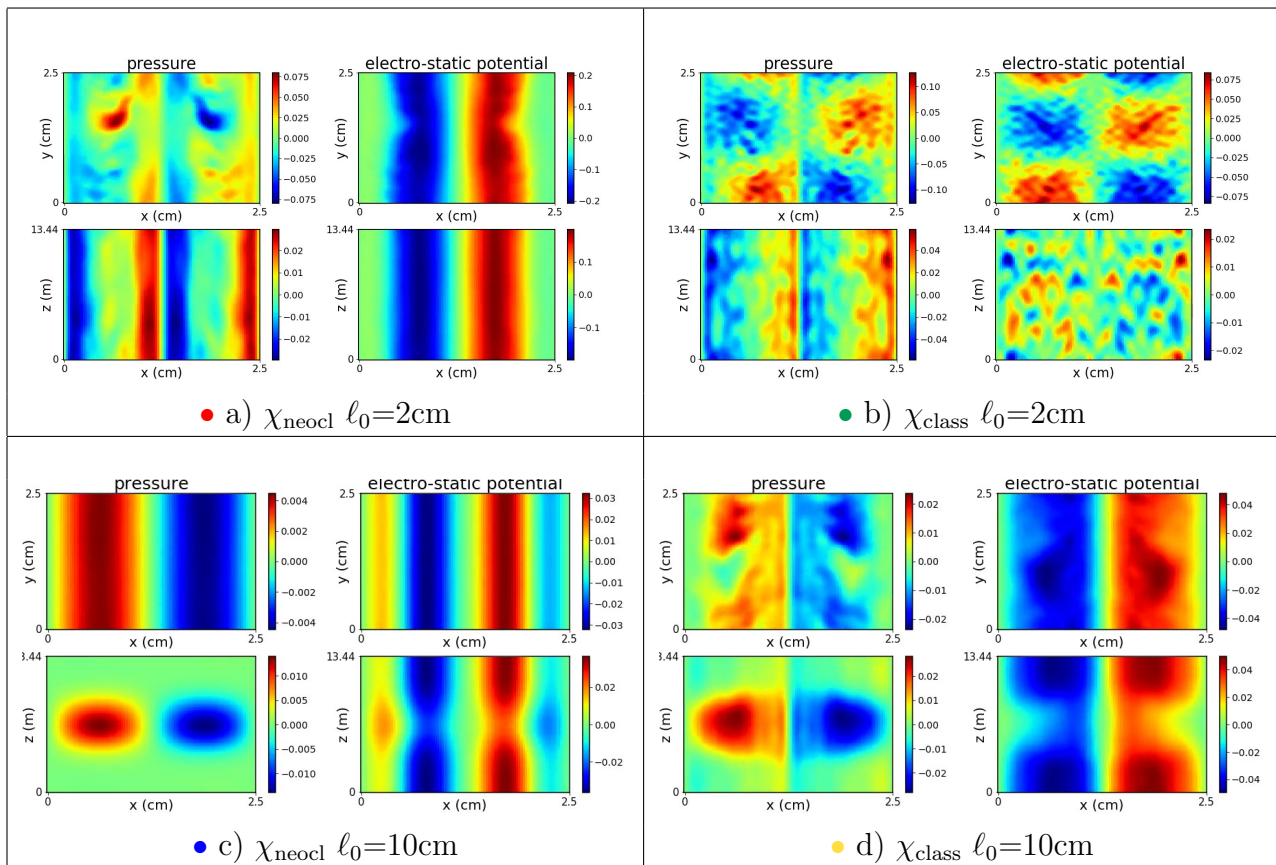


Table 6. The simulation results at time $t = 0.167\text{ms}$ for radially sheared poloidal magnetic field and vanishing radial Dirichlet BC. In each panel the figures above contain the poloidal sections, (x, y) plane, of normalized \tilde{p} (left) and ϕ (right) while the figures below are for the radial-toroidal (x, z) plane. The corresponding colorbars are shown next to each plot.

more intense than in Fig.20. In case d) (yellow), the $E_{\tilde{p}}$ energy spectrum is stiffer with respect to the reference curve (dark yellow) and it resembles the profile for a decaying turbulence scenario. In fact, now turbulence gets reduced, differently from the case with fully periodic BC, and it is not able to sustain the pressure profile that decays in time for both cases c) and d). Since such dissipative phase is diffusivity dominated the fraction of $n = 0$ modes stays almost constant.

This is confirmed by the flux analysis for \tilde{p} , while that for ϕ provides similar results as for fully periodic BC with 2D and toroidal transitions and the linear contributions having similar magnitudes and all contributing to the relaxation to the final energy spectra.

Therefore, implementing vanishing radial Dirichlet BC has a direct impact on the degree of toroidal and poloidal symmetry of the final field configurations, especially for \tilde{p} , on the anisotropy of energy spectra and also on the fate of the saturated \tilde{p} profile, if stationary or time-decaying.

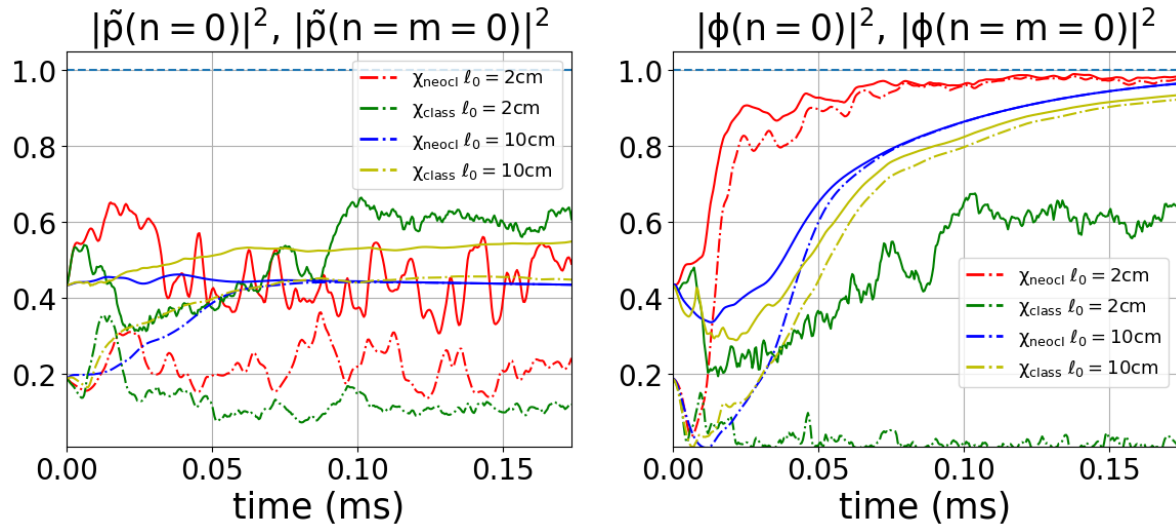


Figure 25. The ratio of $n = 0$ (solid lines) and of $n = m = 0$ (dash-dotted lines) mode amplitudes over the total amplitude for \tilde{p} (left) and ϕ (right) vs time (in ms) for the four considered cases with radially sheared poloidal magnetic field and vanishing radial Dirichlet BC.

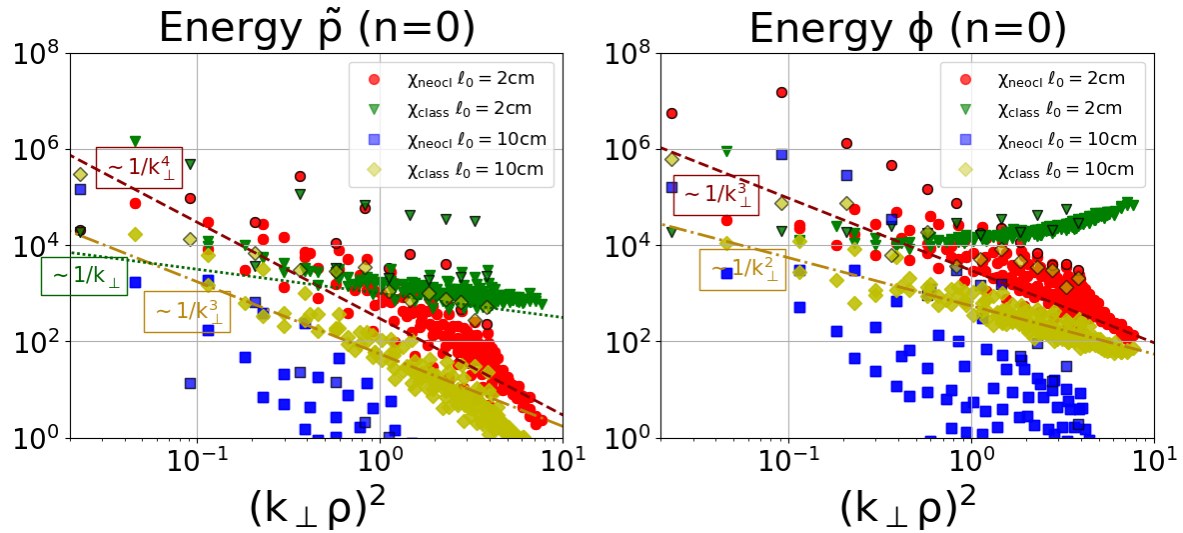


Figure 26. The scatter plots of normalized axisymmetric spectral energies $E_{\tilde{p}}$ (left) and E_{ϕ} (right) vs $(k_{\perp}\rho)^2$ for the four considered cases with radially sheared poloidal magnetic field and vanishing radial Dirichlet BC. They are computed by averaging over a time window of $\sim 0.13ms$. Black edges are for those points corresponding to $m = 0$ modes ($k_y = 0$). For reference some curves are also plotted that approximate quite well some of the spectra profiles in SLAB (see Figs.4 and 9) and which behave as: $1/k_{\perp}^4$ (dashed dark red line), $1/k_{\perp}^3$ (dash-dotted dark yellow line) and $1/k_{\perp}$ (dotted dark green line) for $E_{\tilde{p}}$ (left) and $1/k_{\perp}^3$ (dashed dark red line) and $1/k_{\perp}^2$ (dash-dotted dark yellow line) for E_{ϕ} (right).

4. Conclusions

The simulations for the system of equations (5) describing drift turbulence in the edge of a DTT-like tokamak plasma have been presented. We outlined the rich phenomenology of the resulting 2D energy spectra whose profiles are affected by the choice of model parameters (background pressure gradients and diffusivity), the magnetic geometry (the expression of the poloidal magnetic component in addition to the toroidal one), the radial BC (periodic vs vanishing Dirichlet ones).

The choice of the model parameters determines the relevance of different mechanisms affecting the final field configuration and, in particular, the degree of toroidal symmetry. The magnitude of background pressure gradient, modeled by the inverse of ℓ_0 , determines the amount of \tilde{p} free-energy injected into the system. Such free-energy is subject to a direct toroidal cascade, thus by increasing background pressure gradient, *i.e.* reducing ℓ_0 , one gets more toroidally asymmetric $n \neq 0$ modes. However, the cascade decreases by increasing diffusivity χ_\perp from classical to neoclassical values, that provides major dissipation at large perpendicular scales and minor energy available for the direct toroidal cascade and subsequent transfer to E_ϕ . We discussed two cases for ℓ_0 : weak, $\ell_0 = 10cm$, and strong $\ell_0 = 2cm$ background pressure gradients. For strong gradients, the cases with classical and neoclassical diffusivities differ just quantitatively, with the former showing more toroidal symmetry and more narrow spectra with respect to the latter. For weak gradients, we found in all the considered magnetic configurations a substantial difference between classical and neoclassical χ_\perp : in the latter turbulence is time-decreasing, a sheared radial electric field develops and field profiles show maximal degree of toroidal symmetry. The classical case is qualitatively similar to those with strong gradients and in SLAB we recover the spectral profile $\sim 1/k_\perp^2$ of 2D inviscid Euler equation derived in the reduced model of Ref.[28]. The crucial role of the diffusivity parameter for the emerging turbulent scenario and field spectral features suggests that such parameter should be chosen with great caution in simulations and maybe it is worth planning some diagnostics to measure directly some (pressure and/or potentials) spectral profiles in order to validate our model assumptions (or the findings of consistent models for diffusion such as the $\kappa - \epsilon$ model [19]).

The addition of a poloidal magnetic component to the toroidal one produced strongly anisotropic 2D spectra with more energy for small ms . This is ascribed to the poloidal component of the drift term, that provides an effective dissipative contribution vanishing at $m = 0$ and increasing with m . The resulting spectra for a magnetic configuration that is radially sheared between SLAB and one with a constant poloidal component exhibit anisotropic features due to the poloidal drift and average profiles that roughly follows those in SLAB. The simulations for the X-point magnetic geometry will be presented in the companion paper [45] and the achievements of this work will be used to interpret the results.

A further source of spectral anisotropy is here given by the choice of vanishing radial Dirichlet BC, instead of fully periodic ones, that breaks the formal symmetry

between radial and poloidal coordinates, resulting in a mild enhancement of $m = 0$ modes, mostly for \tilde{p} , and in turbulence quench. Understanding the role of BC and their spectral implications could be relevant to solve the discrepancy between global simulations and experiments in the divertor region, where sheat BC are imposed at the divertor plates. For this reason, further developments will deal with the implementation of sheat BC, via the penalization technique (as in GDB [46] and GRILLIX [18]) or by mimicking the procedure adopted in Refs.[47, 48] to implement nontrivial BC with FFT.

The analysis of fluxes clearly pointed out that toroidal cascades and 2D transitions cannot be treated independently as they are strongly correlated and they provide contributions of the same order that sum up with linear ones to drive the system towards the saturated spectral profiles. This means that 3D simulations are inescapable in order to account for the dynamical features of drift turbulence, as argued by the pioneering work [25].

The inclusion of other drift effects, in particular the curvature contribution accounting for interchange instability, of the diamagnetic velocity, whose role in triggering oscillations is outlined in Ref.[49], and the investigation of magnetic fluctuations via the solution of the electro-magnetic system of equations (1) will be pursued in the follow-up analyses. The aim is to understand the relevance of the present achievements for a complete description of edge tokamak turbulence in view of a comparison with fully-poloidal simulations that could help distinguishing spatially local from global effects.

References

- [1] Ding S *et al* 2024 “A high-density and high-confinement tokamak plasma regime for fusion energy” *Nature* <https://doi.org/10.1038/s41586-024-07313-3>
- [2] Mantica P *et al* 2020 Progress and challenges in understanding core transport in tokamaks in support to ITER operations *Plasma Phys. Control. Fusion* 62 014021
- [3] Mishchenko A *et al* 2023 Numerical tools for burning plasmas *Plasma Phys. Control. Fusion* 65 064001
- [4] Pitcher C S and Stangeby P C 1997 Experimental divertor physics *Plasma Phys. Control. Fusion* 39 779
- [5] Albanese R *et al* 2019 Design review for the Italian Divertor Tokamak Test facility *Fusion Eng. Des.* 146 194
- [6] Ambrosino R 2021 DTT - Divertor Tokamak Test facility: A testbed for DEMO *Fusion Eng. Des.* 167 112330
- [7] Braginskii S I 1965 Transport processes in a plasma *Reviews of Plasma Physics* vol 1, ed A M A Leontovich (New York: Consultants Bureau) pp 205–311
- [8] Simakov A N and Catto P J 2004 Drift-ordered fluid equations for modelling collisional edge plasma *Contr. Plasma Phys.* 44 83
- [9] Shanahan B W and Dudson B D 2014 X-point modelling in linear configurations using BOUT++ *J. Phys.: Conf. Ser.* 561 012015
- [10] Halpern F D *et al* 2016 The GBS code for tokamak scrape-off layer simulations *J. Comput. Phys.* 315 388
- [11] Tamain P *et al* 2016 The TOKAM3X code for edge turbulence fluid simulations of tokamak plasmas in versatile magnetic geometries *J. Comput. Phys.* 321 606

- [12] Stegmeir A *et al* 2018 GRILLIX: a 3D turbulence code based on the flux-coordinate independent approach *Plasma Phys. Control. Fusion* 60 035005
- [13] Schwander F *et al* 2024 Global fluid simulations of edge plasma turbulence in tokamaks: A review *Computers & Fluids* 270 106141
- [14] Oliveira D S *et al* 2022 Validation of edge turbulence codes against the TCV-X21 diverted L-mode reference case *Nucl. Fusion* 62 096001
- [15] Giacomini M *et al* 2022 The GBS code for the self-consistent simulation of plasma turbulence and kinetic neutral dynamics in the tokamak boundary *J. Comput. Phys.* 463 111294
- [16] Mancini D *et al* 2024 Self-consistent multi-component simulation of plasma turbulence and neutrals in detached conditions *Nucl. Fusion* 64 016012
- [17] Quadri V *et al* 2024 Self-organization of plasma edge turbulence in interaction with recycling neutrals *Contr. Plasma Phys.* e20230014
- [18] Stegmeier A 2019 Global turbulence simulations of the tokamak edge region with GRILLIX *Phys. Plasmas* 26 052517
- [19] Bufferand H *et al* 2021 Progress in edge plasma turbulence modelling—hierarchy of models from 2D transport application to 3D fluid simulations in realistic tokamak geometry *Nucl. Fusion* 61 116052
- [20] Zholobenko W *et al* 2021 Electric field and turbulence in global Braginskii simulations across the ASDEX Upgrade edge and scrape-off layer *Plasma Phys. Control. Fusion* 63 034001
- [21] Hasegawa A and Wakatani M 1983 Plasma Edge Turbulence *Phys. Rev. Lett.* 50 682
- [22] Wakatani M and Hasegawa A 1984 A collisional drift wave description of plasma edge turbulence *Phys. Fluids* 27 611
- [23] Hasegawa A and Wakatani M 1987 Self-organization of electrostatic turbulence in a cylindrical plasma *Phys. Rev. Lett.* 59 1581
- [24] Hasegawa A and Mima K 2018 Strong turbulence, self-organization and plasma confinement *Eur. Phys. J. H* 43 499
- [25] Biskamp D and Zeiler A 1995 Nonlinear Instability Mechanism in 3D Collisional Drift-Wave Turbulence *Phys. Rev. Lett.* 74 706
- [26] Scott B D 2002 The nonlinear drift wave instability and its role in tokamak edge turbulence *New J. Phys.* 4 52
- [27] Scott B D 1990 Self-Sustained Collisional Drift-Wave Turbulence in a Sheared Magnetic Field *Phys. Rev. Lett.* 65 3289
- [28] Montani G, Carlevaro N and Tirozzi B 2022 On the Turbulent Behavior of a Magnetically Confined Plasma near the X-Point *Fluids* 7 157
- [29] Montani G and Carlevaro N 2023 On the 3D turbulence regime in a Tokamak plasma edge *Physica D* 451 133774
- [30] Carlevaro N, Montani G and Moretti F 2023 On the Effects of Tokamak Plasma Edge Symmetries on Turbulence Relaxation *Symmetry* 15 1745
- [31] Diamond P H *et al* 2005 Zonal flows in plasma—a review *Plasma Phys. Control. Fusion* 47 R35
- [32] Diamond P H *et al* 2011 Vorticity dynamics, drift wave turbulence, and zonal flows: a look back and a look ahead *Plasma Phys. Control. Fusion* 53 124001
- [33] Burrell K H 2020 Role of sheared $E \times B$ flow in self-organized, improved confinement states in magnetized plasmas *Phys. Plasmas* 27 060501
- [34] Vermare L *et al* 2020 Formation of the radial electric field profile in the WEST tokamak *Nucl. Fusion* 62 026002
- [35] Hidalgo C *et al* 2006 Physics of sheared flow development in the boundary of fusion plasmas *Plasma Phys. Control. Fusion* 48 S169
- [36] Long T *et al* 2019 Studies of Reynolds stress and the turbulent generation of edge poloidal flows on the HL-2A tokamak *Nucl. Fusion* 59 106010
- [37] Connor J W 1973 The neo-classical transport theory of a plasma with multiple ion species *Plasma Phys.* 15 765

- [38] Kendl A and Scott B D 2003 Magnetic Shear Damping of Dissipative Drift Wave Turbulence *Phys. Rev. Lett.* 90 035006
- [39] Beyer P, Garbet X and Ghendrih P 1998 Tokamak turbulence with stochastic field lines *Phys. Plasmas* 5 4271
- [40] Bowman J C and Roberts M 2011 Efficient dealiased convolutions without padding *SIAM J. Sci. Comput.* 33 386
- [41] Kraichnan R and Montgomery D 1980 Two-dimensional turbulence *Rep. Prog. Phys.* 43 547
- [42] Numata R, Ball R and Dewar R L 2007 Nonlinear Simulation of Drift Wave Turbulence *Phys. Plasmas* 14 102312
- [43] Scott B D 2007 Tokamak edge turbulence: background theory and computation *Plasma Phys. Contr. Fus.* 49 S25
- [44] Saffman P G 1971 On the Spectrum and Decay of Random Two-Dimensional Vorticity Distributions at Large Reynolds Number *Stud. Appl. Math.* 50 377
- [45] Cianfrani F and Montani G “Turbulent features near the X point of a DTT-like tokamak plasma”, in preparation
- [46] Zhu B, Francisquez M and Rogers B N 2018 GDB: A global 3D two-fluid model of plasma turbulence and transport in the tokamak edge *Comput. Phys. Commun.* 232 46
- [47] To Q D, Bonnet G and Nguyen-Thoi T 2021 Fourier transform approach to nonperiodic boundary value problems in porous conductive media *Int. J. Numer. Methods Eng.* 122 4864
- [48] Wang Q *et al* 2020 FFT-Based Methods for Computational Contact Mechanics *Front. Mech. Eng.* 6 61
- [49] Cianfrani F, Fuhr G and Beyer P 2022 Edge plasma relaxations due to diamagnetic stabilization *Phys. Plasmas* 29 032302